

A Railway Accident Prevention System Using An Intelligent Pilot Vehicle

Shixiong Wang, Xinkle Li, Zhirui Chen, and Yang Liu

Abstract—Railway transportation, as a pillar of modern civilization, unavoidably suffers from external risk factors such as natural disasters, track breakages, and train collisions, which lead to substantial loss of life and property. Hence, it is urgent to design a mechanism to warn and prevent railway accidents to diminish the costs. We propose an add-on solution to the current system, which equips a train with a multifunctional pilot vehicle in the front: the vehicle pilots its mother train, warning it of impending danger, and stopping it if required. Specifically, the pilot vehicle is equipped with a wireless communication device to converse with the mother train, a ranging device to measure the real-time distance from the mother train, a camera to capture the railway conditions ahead and recognize anomaly situations, and other sensors (e.g., collision detector and tiltmeter) to monitor its own conditions. Based on the above equipment, an efficient autonomous driving method is designed for the pilot vehicle to adjust the distance from the train. The autonomous driving problem can be formulated into a multi-objective functional optimization, where the objective is to minimize the total energy consumption and the experienced jerk of the pilot vehicle, and the decision is a continuous-time function that represents the traction or braking force imposed on the pilot vehicle. Additionally, a vision-based deep learning method is devised to automatically detect the mentioned railway anomalies using the ego-view camera of the pilot vehicle. To control the operational and maintenance costs, we propose to deploy pilot vehicles only for trains running in potentially dangerous environments, e.g., mountainous areas during rainy days. By applying the scheme presented, we expect that the accident rates of the railway systems can be reduced.

Index Terms—Intelligent Transportation, Railway Accidents, Autonomous Driving and Control, Multi-objective Functional Optimization, Anomaly Detection, Deep Neural Network.

I. INTRODUCTION

Due to the critical role that railway transportation plays in modern civilization, railway accidents, once they occur, always lead to substantially severe consequences, such as loss of human life, damage to the environment, and disruption of economic activities. Train collisions and derailments are the most common types of severe railway accidents, and they may be caused by various factors. Specifically, train collisions, which occur between operating trains and barricades,

humans, or other trains, are often caused by landslides or mudslides, trespassing, and dysfunction of scheduling systems, respectively. In contrast, derailments are mainly induced by track distortions or breakages, and these track issues might be caused by equipment aging, earthquakes, terrorism, and so on. Until today, railway accidents, including train collisions and derailments, are still intensively reported worldwide from the U.S. [1] to India [2], to China [3], [4]. For example, in the past decade, the U.S. has reported 7,786 deaths and 80,248 non-fatal injuries attributed to railroad transportation accidents.¹ So far, significant efforts have already been made to prevent train accidents by addressing controllable factors such as dysfunction of scheduling systems and misoperation of train drivers [5], [6], [7], [8], [9]. Typical solutions include Positive Train Control (PTC) systems [10], [11], [12] and Communication-Based Train Control (CBTC) systems [13].² However, the safety issues in railway transportation resulting from uncontrollable factors remain unresolved, including landslides or mudslides, trespassing, especially not at grade crossings,³ equipment aging, earthquakes, and terrorism. Hence, there is a great interest in finding a more comprehensive railway accident prevention scheme working in various circumstances, and the scheme is expected to be compatible with existing railway infrastructures.

In current practice, several strategies have been presented for railroad accident prevention at the system level. Common preventive measures for railway accidents are carried out through routine maintenance by ad-hoc inspection vehicles [15], [16] and the construction of physical barriers [17]. The former refers to the daily inspection procedure where rail tracks undergo a set of maintenance schedules to prevent accidents associated with track failures (e.g., track distortions, track tilts, and track breakages), while the latter implies physical fences that encircle railway systems to reduce human-element risks such as trespassing. Although these measures do showcase their usefulness nowadays, they fail to inspect railway conditions in a real-time manner and are, therefore, unable to respond to many emergencies. For example, periodic railway inspection by ad-hoc vehicles is not sufficient to respond promptly to cloudbursts or other sudden climate events in mountainous areas. For another example, unexpected trespassers or suicides can climb rail fences, requiring the

S. Wang and X. Li contributed equally to this paper.

Y. Liu is the corresponding author.

S. Wang, X. Li, and Z. Chen are with the Department of Industrial Systems Engineering and Management, National University of Singapore. Y. Liu is with the Department of Civil and Environmental Engineering and the Department of Industrial Systems Engineering and Management, National University of Singapore. (E-mail: s.wang@u.nus.edu; xinke.li@u.nus.edu; zhiruichen@u.nus.edu; iseliuy@nus.edu.sg).

This work was supported by Singapore Ministry of Education Academic Research Fund Tier 2 (MOE2019-T2-2-165).

¹See “Section 1.12 - Ten Year Accident/Incident Overview” at <http://safetydata.fra.dot.gov/OfficeofSafety/>, issued by the Office of Safety Analysis, Federal Railroad Administration.

²CBTC is an expansive version of PTC [10].

³Trespassing at grade crossings can be monitored by cameras [14] and prevented by PTC systems [10, p. 5].

installation of a real-time surveillance system capable of notifying and braking running trains.

With the rapid development of sensing technology, an alternative to current accident prevention measures is to hire cutting-edge sensors on the railway system [18], [19]. In the literature, two types of deployment strategies for sensors are reported. One is the on-board strategy, where sensors are installed on the locomotives of trains [19], while the other is the wayside strategy, where sensors are placed on (or near) railways [18]. On-board sensors such as LiDARs and cameras are the first to be fitted to the train system. However, the sensors' limited range prevents them from warning train operators or operational systems of approaching threats at a greater distance, e.g., one kilometer. Especially in light of the increasing popularity of high-speed trains, the sensing distance does not guarantee that the train will be able to act on warnings effectively in time. A plausible upgrade to on-board sensors is the establishment of wayside wireless sensor networks (WSNs), which monitor all-around and real-time railway conditions [20], [18], [21]. WSNs consist of autonomous and spatially distributed sensors that cooperatively monitor the railway infrastructure, structures, and operations, allowing early detection of possible accidents. The monitoring data are individually collected by each sensor and transferred to remote servers for centralized processing [20]. However, two issues have to be noted. The major one is the high cost of deploying large-scale sensor networks (although they are inexpensive per sensor unit) and building wireless communication infrastructures to cover all existing railway systems. The second one is to design robust and reliable sensor powering, maintenance, and replacement schemes, which is difficult considering the bulky size of WSNs and the harsh natural circumstances in some railway lines [22].

To address the above concerns about the prevention of railway accidents, motivated by vehicle platooning problems [23], [24], we propose a novel and flexible scheme for upgrading the current rail transportation system by using multifunctional pilot vehicles. In this scheme, a pilot vehicle acts as a navigator for each train, exploring the train's route ahead. Specifically, when there is an accident risk on the railway, the pilot vehicle warns its mother train of the danger and, if required, instructs the train to halt promptly. Such pilot vehicles are more cost-flexible than installing WSNs since they may be used exclusively on operating trains and not on standby ones. Also, they can be employed solely on railway lines with a high risk of accidents, e.g., mainlines in mountainous areas during rainy days. On the other hand, compared with WSNs' maintenance difficulty due to large coverage areas, the suggested scheme enables frequent maintenance and replacement of pilot vehicles at railway terminals, resulting in a higher level of functional reliability. Admittedly, it is promising to jointly adopt our scheme and existing WSN solutions in an appropriate and ad hoc way, further improving the sensitivity and timeliness of railway accident detection. However, this side problem is beyond the scope of this paper.

In the following contexts, we first propose a system architecture for the pilot vehicle and the method to integrate it into current railway transportation. Then, specific technologies

for the pilot vehicle, such as autonomous driving and vision-based anomaly detection methods, are investigated. The autonomous driving method is designed for the pilot vehicle to automatically adjust its distance from the mother train, while the vision-based anomaly detection method is used to monitor the railway conditions ahead in a real-time manner. With this systematic approach, we expect railway accidents worldwide could be avoided or at least controlled. However, it is possible that some new safety issues will be introduced when using the proposed solution. For example, the pilot vehicle might lose reliable communication with its mother train in some rare cases (e.g., anomalies in the communication devices), so that the train would collide with its pilot vehicle. Nevertheless, we believe that this kind of collision costs are significantly less than the usual railway accidents because the safety of humans is the first concern, and the mass (i.e., inertia) of the pilot vehicle is small. Besides, if some buffering devices between the pilot vehicle and its mother train are used, the collision risks can be further controlled. Furthermore, the vision-based railway inspection method may not work robustly at night or in extremely bad weather conditions (e.g., heavily rainy and foggy). However, it causes no disasters because we have functionally supplementary sensors to collaboratively detect railway anomalies.

Parallel to this paper, the SMART2 Project [25]⁴ recently envisages another system-level strategy to possibly solve the same problem as this paper does. The difference is that the SMART2 Project proposes to use drones, intensive wayside sensor networks, and on-board sensors to conduct railway anomaly detection and warning. Nevertheless, on the one hand, as explained before, the main issues of this proposal are the considerable cost to cover the huge-scale railway systems and the limited sensing range of on-board sensors; on the other hand, operations involving drones, such as powering, maintenance, and intelligent scheduling and swarming are still challenging, doubting their compatibility with the current railway system. Even if this is not the case, we believe this paper provides flexibility and new motivations for designers of future-generation intelligent railway systems worldwide.⁵ Since the proposed pilot-based accident-prevention mechanism is an add-on solution to the current railway system, we do not require upgrading any of the existing railway infrastructures, for example, installing on-board sensors on locomotives and deploying wayside sensors. In contrast, the SMART2 Project expects to deploy on-board sensors (for trains) and wayside sensors, and therefore, it is not an add-on and compatible solution. This is a promising feature for countries that are not free of upgrading their existing railway infrastructures and existing trains.

The contributions of this paper are summarized below.

- 1) We provide a systematic solution blueprint for the railway safety-guaranteeing problem. The sensor deployment and information streaming strategies to realize such a system are discussed. See Section II and Figs. 1, 2;

⁴For more, see the project's homepage at <https://smart2rail-project.net>.

⁵Note that the SMART2 Project is in the designing process and has not been practically implemented.

- 2) We present an autonomous driving method for the pilot vehicle; See Section III and Figs. 5, 6, and 7. In highlights,
- The relative distance profile between the mother train and the pilot vehicle is designed based on a multi-objective functional optimization where the decision variable is the traction or braking force for the pilot vehicle (i.e., a time function). The objective is to minimize the relative acceleration and deceleration distances of the pilot vehicle, the total energy required for the pilot vehicle, and the total jerks that the pilot vehicle experiences. See Eqs. (3)~(15).
 - We introduce two second-order cone constraints into the functional optimization so that the traction or braking force for the pilot vehicle is guaranteed to be continuous over time. See (27), (28), (36), and (37);
- 3) We display a vision-based railway anomaly inspection method to detect track failures, landslides and mudslides, and trespassers and workers; See Section IV. In highlights,
- We develop a new deep network called Folded Spatial Convolution Neural Network (FSCNN) for semantic segmentation of real-time captured images in railway scenes. It has higher computational efficiency and achieves better long-range message passing than existing baselines such as the Spatial Convolution Neural Network (SCNN); See Fig. 15;
 - An integrated vision-based railway inspection system is proposed to function the track inspection and obstacle detection. The system works with the railway vision segmentation results from FSCNN; See Fig. 14.
 - A new evaluation dataset, named RailInspect, of railway anomaly inspection has been created, which addresses the scarcity of publicly available datasets. The results obtained using RailInspect demonstrate the practicality and the effectiveness of the proposed inspection system.

The paper is organized as follows. In Section I, we provide the problem background and highlight the overall contributions of this paper. In Section II, the pilot-vehicle-based framework to guarantee railway safety is proposed. The autonomous driving method for the pilot vehicle is designed in Section III, and the vision-based railway anomaly inspection system is presented in Section IV. The conclusions in Section V complete this paper.

II. SYSTEM DESIGN

The whole view of the pilot-based accident-prevention mechanism is shown in Fig. 1.

A. System Integration

The pilot vehicle is mainly equipped with (a) a collision detection device to detect the collisions between the pilot vehicle and landslides or mudslides, or another train; (b) a camera to capture the railway conditions ahead and to identify the track distortions, track breakages, trespassing humans, railway workers, landslides, and mudslides using deep learning methods; (c) a communication device to exchange information



Fig. 1. The 3-dimensional (3D) illustration of the whole system. The small yellow vehicle (left) is the pilot vehicle running ahead of its mother green train (right). The pilot vehicle can be seen as the soft-connected virtual locomotive of the mother train. The model is created by Cinema 4D (<https://www.maxon.net/en/cinema-4d>).

with its mother train; (d) a line-of-sight ranging device to measure the real-time relative distance from the train; (e) a side-pressure sensor installed on wheels to monitor the track status, i.e., whether the track is deformed; and (f) an inertial unit (e.g., gradiometer and gyroscope) or a tiltmeter to monitor whether the track is tilted. The sensors are **functionally supplementary**, so reliability can be further controlled. For example, even when the camera is out of work, e.g., in very foggy weather conditions, the side-pressure sensor and the front collision detector can still perceive dangers. The converse is true as well. The pilot vehicle is an autonomous one so it can intelligently maintain a safe distance from the train.

A close-up of the pilot vehicle is available in Fig. 2 (a). In Fig. 2 (b), the positions to place the mentioned sensors are illustrated.

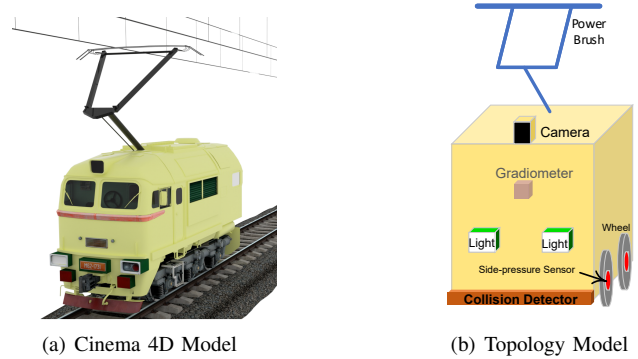


Fig. 2. The 3D illustration of the pilot vehicle. In (b), a gradiometer or a tiltmeter is installed inside the vehicle.

Remark 1: As a replacement for the line-of-sight ranging device (e.g., radar and laser [26]) to measure the real-time relative distance between the pilot vehicle and its mother train, the wayside positioning devices (e.g., balises [7]) could be utilized to obtain the real-time positions of the pilot vehicle and the train and then decide the relative distance. To be specific, for example, when the train and the pilot vehicle pass by wayside balises, electromagnetic readers installed on the train and the pilot vehicle can query balises about the current positions because balises know their own installation positions on the track. Through this, the relative distance between the train and the pilot vehicle can be determined.

Note that in this case, the positioning accuracy depends on the installation density of the balises on the track. When the installation density is high (e.g., one per meter), the accuracy and reliability of such a positioning scheme are high. The benefit of using balises is that the relative distance along curved tracks can also be obtained. \square

Remark 2: GNSS (global navigation satellite system) receiver is not deployed for the pilot vehicle to obtain the real-time position because in mountains or tunnels (e.g., China's Longhai Railway) or in rainy or foggy environments, the GNSS signal is so weak that it may not be reliable enough to precisely locate the carrier. Therefore, for the safety guarantee purpose, it is better to measure and utilize the relative distance between the pilot vehicle and its mother train. \square

Remark 3: The proposed method is an add-on solution without requiring changes or upgrades of existing railway infrastructures and trains. \square

B. Information Streams

Since the focus of this paper is not on the mother train, we assume that reliable information about the train, such as real-time positions and velocities, is known [5], [27], [6].

At any time, the ranging device can obtain the relative distance (along the track) between the pilot vehicle and its mother train. Using this relative distance, the pilot vehicle could maintain a safe distance from the train. When a straight-line ranging device is used, if the pilot vehicle is outside the line-of-sight area of the train, the straight-line ranging device cannot provide relative distance anymore.⁶ In this case, the train and the pilot vehicle use wireless communication devices to exchange information with each other. Specifically, the train transmits its real-time velocity to the pilot vehicle. The pilot vehicle utilizes its autonomous driving system to infer the current relative distance and maintain it within a safe range. This temporary dead-reckoning strategy would not cause a disaster because most parts of a railway are (nearly) straight.

By jointly using the vision-based inspection method, collision detector, and side pressure sensor, if the pilot vehicle identifies any dangers (no matter existing or latent), it transmits the warning message to the train or directly commands the train to brake. Meanwhile, the railway conditions can be sent to the train operator via an image stream. The warning is also triggered if the tiltmeter installed in the pilot vehicle detects any tilt on the track (i.e., the left track is significantly higher than the right, or the converse).

C. System Functioning

After depicting the hardware structure of the pilot vehicle (Fig. 2) and its integration method into the current railway system (Fig. 1), to function the proposed pilot-based accident-prevention mechanism, the following steps are to design the autonomous driving method and anomaly inspection method for the pilot vehicle, which are the software part of the proposed mechanism and discussed in Sections III and IV,

⁶Recall from Remark 1 that when wayside positioning devices such as balises are used, directly measuring the relative distance along curve tracks is possible.

respectively. In this sense, the contents in Sections III and IV would be technically unrelated. However, they are highly related at the system level: they complementarily enable the function of the proposed pilot-based accident-prevention mechanism. An illustration is given in Fig. 3. Specifically, the pilot vehicle is supposed to conduct scene perception (i.e., analysis of signals and images from different sensors such as the collision detector and the camera) and distance control from its mother train (i.e., autonomous driving). The pilot vehicle is also expected to send real-time visual information to the driver of its mother train for his information and to generate brake and warning messages.

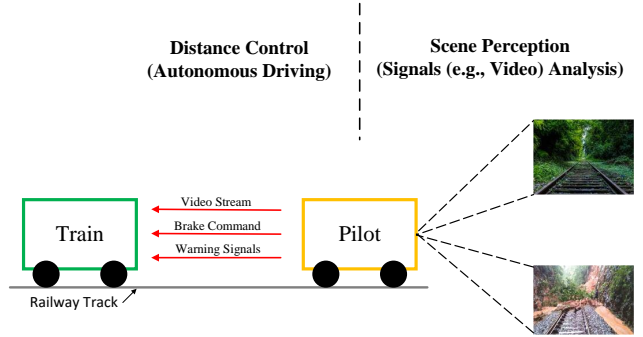


Fig. 3. The pilot vehicle navigates its mother train; the pilot vehicle can be seen as the soft-connected virtual locomotive of the mother train. The pilot vehicle is supposed to conduct scene perception and distance control (from its mother train). The pilot vehicle sends visual information to the train's driver and generates brake and warning messages.

III. AUTONOMOUS DRIVING OF THE PILOT VEHICLE

In this section, we design the autonomous driving method for the pilot vehicle to dynamically adjust the relative distance from its mother train. Specifically, we expect the distance between the pilot vehicle and its mother train to be sufficiently small near the stations to save space, and to be sufficiently large during a trip to guarantee railway safety. The autonomous driving problem is technically an optimal control problem where the power supply system of the pilot vehicle dynamically changes the traction or the braking force imposed on the pilot vehicle to dynamically control the relative distance between the pilot vehicle and its mother train. This optimal control problem can be mathematically formulated into a multi-objective functional optimization where

- 1) the decision is a continuous-time function representing the traction or braking force imposed on the pilot vehicle;
- 2) the objective is to minimize the relative acceleration distance and the relative deceleration distance of the pilot vehicle, the total energy required for the pilot vehicle, and the total jerk that the pilot vehicle experiences during a trip;
- 3) the constraints include the dynamics and kinematics of the pilot vehicle and some boundary conditions (e.g., minimum safety distance between the pilot vehicle and its mother train, maximally allowed velocity difference between the pilot vehicle and its mother train, maximally allowed traction and braking forces). In addition, we introduce two

second-order cone constraints so that the decision (i.e., the traction or braking force) is guaranteed to be a continuous function over time.

Afterward, the multi-objective functional optimization problem is decomposed into two functional sub-problems that can be independently solved using the pseudo-spectral method. Finally, controllers such as PID controllers are used to let the power supply system drive the pilot vehicle so that the pilot vehicle can follow the relative distance profile predesigned by the multi-objective functional optimization.

A. Problem Formulation

Suppose we investigate a train travelling from station A to station B; see Fig. 4. We aim to design a suitable time function x_{ref} as a reference for x . During the trip, the pilot vehicle tries to use an efficient control algorithm to let x track x_{ref} as accurately as possible. In other words, the smaller the difference between the expected x_{ref} and the real-time measured x , the better. The control scheme of autonomous driving is shown in Fig. 5. In detail, firstly, the mother train transmits its real-time velocity v_m and position p_m to the autonomous driving system that also simultaneously receives the real-time relative distance x from the ranging device; secondly, the autonomous driving system compares the tracking error (between x_{ref} and x) and generates the expected traction or braking force signal u_{ref} for the power system of the pilot vehicle to execute; thirdly, the power system outputs the real traction or braking force u to drive the pilot vehicle, during which u_{ref} and u are expected to be as close as possible (so that x_{ref} and x would be as close as possible).

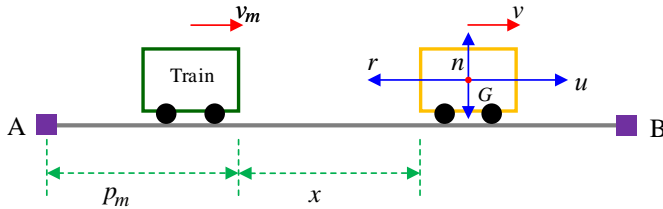


Fig. 4. The pilot vehicle and its mother train (only the locomotive displayed) are running from station A to station B. The relative geometry of the system and the force analysis of the pilot vehicle are shown. The distance (along the track) to the train from station A is P_m ; the relative distance from the pilot vehicle to the train is x ; the velocity of the train is v_m and of the pilot vehicle is v . Four types of forces are acting on the pilot vehicle: the traction or braking force u (negative when braking), the resistance r , the support n , and the gravity G .

Remark 4: In this study, we do not take into consideration the automatic train operation (ATO) problem of the mother train. Instead, we suppose that the speed-distance profile of the mother train is already determined [7], [28], [29] and we focus only on the autonomous control of the pilot vehicle. In addition, we assume that the autonomous driving system of the pilot vehicle can obtain the real-time velocity v_m and position p_m of the mother train via the communication channel. \square

A proper reference signal x_{ref} should satisfy the following criteria:

- 1) It is small (e.g., within 10 meters or even 0 meters) when the train parks at, starts departing from or approaching its

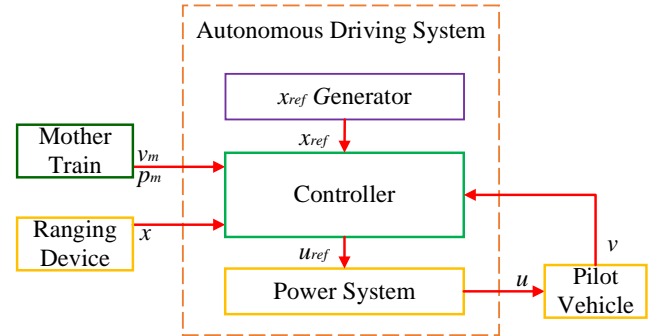


Fig. 5. The control scheme of the autonomous driving system for the pilot vehicle. The controller continuously compares the difference between the expected x_{ref} and the real-time measured x , and then generates the command signal u_{ref} (viz., traction or braking force) for the power system to execute. Physically, the ranging device and the autonomous driving system are all installed on the pilot vehicle.

stations. This is to limit the space occupied by a train at a station;

- 2) It is larger than the emergency braking distance of the mother train (which is usually at least 800 meters) when the train is running between the two stations;
- 3) It requires as few as electrical energy from the railway power supply system. This is to save energy and reduce the emission of greenhouse gases (e.g., carbon dioxide);
- 4) It acts as few as jerks (i.e., few sudden changes in u) on the pilot vehicle. This is to protect the pilot vehicle from mechanical shocks and wears.

B. System Dynamics

In order to perform perfect tracking of x_{ref} , we need to study the system dynamics of the pilot vehicle **along the track**. Fig. 4 shows the forces acting on the pilot vehicle. The traction or braking force u is from the power system (negative when braking). The resistance r consists of four parts: (a) mechanical rolling resistance r_r ; (b) aerodynamic drag r_d ; (c) gradient resistance r_g ; and (d) curve resistance r_c [30], [7], [31]. According to the Davis formula [32], the rolling and aerodynamic resistance can be jointly expressed in terms of velocity v and mass m as

$$r_{r,d} = r_r + r_d = m \cdot (c_0 + c_1 v + c_2 v^2), \quad (1)$$

where c_0 , c_1 , and c_2 are constant coefficients for a given vehicle, which are usually obtained by wind tunnel tests [33]. Besides, the gradient resistance r_g and curve resistance r_c can be given in terms of the gradient angle θ and track curve radius ρ as $r_g = mg \sin \theta$ and $r_c = mg \cdot 700/\rho$ [30], [31], respectively, where g denotes the gravity constant ($9.81 N/Kg$). Note that $\theta = \theta(p)$ and $\rho = \rho(p)$ are functions with respect to the position of the pilot vehicle and $p := p_m + x$. Note also that tunnel resistance discussed in [29] can be integrated into $r_{r,d}$; one just needs to adjust the values of c_0 , c_1 , and c_2 along the track. Therefore, neglecting tunnel resistance does not lose the generality of the system's dynamics analysis.

Therefore, according to Newton's second law, we have the system dynamics of the pilot vehicle as

$$\begin{cases} \frac{dx}{dt} = v - v_m \\ \frac{dv}{dt} = \epsilon \frac{u}{m} - c_0 - c_1 v - c_2 v^2 - g \sin \theta - g \frac{700}{\rho}, \end{cases} \quad (2)$$

where ϵ denotes the acceleration coefficient [34]; this is a nonlinear system. Note that the total resistance equals to $r = r_{r,d} + r_g + r_c = m(c_0 + c_1 v + c_2 v^2) + mg \sin \theta + mg \frac{700}{\rho}$. Note also that the forward force generated by the gravity of the pilot when it runs downhill has been implicitly incorporated into (2). Specifically, when the gradient angle θ of the track is positive (i.e., uphill), the value of $-g \sin \theta$ is negative, and it denotes the gradient resistance generated by gravity. However, when the gradient angle θ of the track is negative (i.e., downhill), the value of $-g \sin \theta$ is positive, and it denotes the forward force generated by gravity.

C. Design the Reference Relative Distance

In this subsection, we design a proper reference relative distance profile x_{ref} . Suppose that the train will take time T to travel from station A to station B (T is available from the train's ATO [7]). First, we aim to minimize two criteria for the pilot vehicle:

- 1) Total energy that the pilot requires from the power system, i.e., $E = \int_0^T |u(t) \cdot v(t)| dt$. Note that instantaneous power is defined as the product of instantaneous external force and instantaneous velocity, and the energy is the time integral of the power. Here, we suppose that the power system can output both traction force (positive) and braking force (negative). Since $u(t)$ is negative when actively braking, the absolute function is needed. If the braking force is not generated from the power system but from an independent braking system such as a friction-based braking system [35], we have $u(t) = 0$ when braking.
- 2) Total jerk required, i.e., $J = \int_0^T 1/m \cdot |du(t)/dt| dt$. Note that the jerk $j(t)$ is defined as the derivative of the acceleration with respect to time, i.e., $j(t) := 1/m \cdot du(t)/dt$. We use the integral of the absolute value of the jerk function as the objective because this objective can guarantee the boundedness and continuity of the jerk function $j(t)$. The boundedness and continuity of the jerk function $j(t)$ implies the comfortable riding feelings of passengers and mild mechanical wear of equipment. According to the Riemann-Lebesgue theorem, a bounded function on a compact (i.e., finite and closed) interval is almost everywhere (in the Lebesgue zero-measure sense) continuous if and only if it is Riemann integrable. Therefore, by minimizing the defined integral, the upper bound of the absolute value of the jerk function $j(t)$ is minimized while guaranteeing that the function $j(t)$ is continuous. On the other hand, when the jerk function $j(t)$ is bounded and continuous, the control function $u(t)$ is guaranteed to be smooth; cf., e.g., [36, Eq. (3.4)], [37, Eq. (2.3a)]. A smooth control function $u(t)$ is easier to be generated by the power system with high accuracy. More discussions and experimental verification

on this point can be seen in Appendix A of the online supplementary materials.

Remark 5: In this paper, we assume that the required traction and braking force u , which is negative when braking, for autonomously driving of the pilot vehicle is solely supplied by the conventional power system. However, it is possible to consider the inclusion of the regenerative braking system simultaneously. For example, when the required *braking* force is $u = -1 \times 10^3 N$, it is possible to let the regenerative braking system provide $u_1 = -0.2 \times 10^3 N$ (N.B.: u_1 is generated by the kinetic-to-electrical energy transformation process) and let the usual power system provide the other $u_2 = -0.8 \times 10^3 N$ where $u_1 + u_2 = u$. For another example, when the required *traction* force is $u = 1 \times 10^3 N$, it is possible to let the regenerative braking system provide $u_1 = 0.2 \times 10^3 N$ (N.B.: u_1 is generated by the electrical energy stored in the energy storage device) and let the usual power system provide the other $u_2 = 0.8 \times 10^3 N$ where $u_1 + u_2 = u$. However, how to schedule such braking and traction efforts for the pilot vehicle is beyond the research focus (i.e., accident prevention mechanism design) of this paper—it is a separate research issue; see, e.g., [38], [28], [39] where the design problem of x_{ref} may be of a different optimization formulation. For more notes on this point, see Appendix B of the online supplementary materials. \square

Suppose that when the train is either parked at a station or running in close proximity to it (i.e., approaching or departing), there is a minimum required relative distance, denoted as x_0 (e.g., 20 meters), which should be small to save the station space and prevent potential collisions with other trains. Notably, x_0 can even be set to zero if a precise and soft-contact control system, which is similar to rendezvous and docking in astronautics, and soft landing in aeronautics, is available so that potential collisions between the mother train and the pilot vehicle can be avoided. When the train is running between the two stations, we assume that the maximum relative distance is x_{max} , which must be greater than the safety distance x_s (e.g., 1400 meters), as illustrated in Fig. 6. The following constraints must be ensured:

- 1) Boundary conditions, i.e., $x_{ref}|_{0 \leq p_m \leq p_m^s} = x_0 = const$, $v|_{0 \leq p_m \leq p_m^s} = v_m = v_m(t)$, $x_{ref}|_{p_m^e \leq p_m \leq R} = x_0 = const$, and $v|_{p_m^e \leq p_m \leq R} = v_m = v_m(t)$; see Fig. 6;
- 2) Safety relative distance, i.e., $x_{ref}|_{p_m^c \leq p_m \leq p_m^b} = x_{max} = const > x_s$, $v|_{p_m^c \leq p_m \leq p_m^b} = v_m = v_m(t)$; see Fig. 6;
- 3) Maximum relative velocity, i.e., $v - v_m \leq v_{max}^\Delta, \forall t \in [0, T]$;
- 4) Maximum allowable traction or braking force $-\underline{U} \leq u \leq \overline{U}, \forall t \in [0, T]$, where \underline{U} denotes the maximum braking force and \overline{U} the maximum traction force;
- 5) u is at least continuous at turning points of trip sections, i.e., at p_m^s, p_m^c, p_m^b , and p_m^e , better to be smooth as well. This is to limit the mechanical jerks acting on the pilot vehicle. More importantly, a continuous u is easier for the power system to generate.

Fig. 6 means that in our model, we expect the velocity of the pilot vehicle to follow the velocity of the mother train when $0 \leq p_m \leq p_m^s, p_m^c \leq p_m \leq p_m^b$, and $p_m^e \leq p_m \leq R$

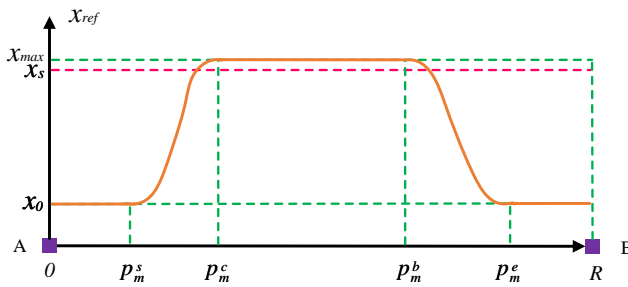


Fig. 6. An illustration of a possible x_{ref} . The relative safety distance (i.e., emergence braking distance) of the mother train is denoted as x_s . The distance (along the track) from station A to B is R . The pilot vehicle maintains the constant relative distance x_0 when the train departs from and approaches its stations to save station space so that latent collisions between the pilot vehicle and other trains could be avoided. The vehicle uses the buffer distance from p_m^s to p_m^c to reach x_{max} from x_0 , and the buffer distance from p_m^b to p_m^e to reach x_0 from x_{max} . Note that in practice, x_{max} and x_s have almost the same value. The superscript i of p_m^i labels the notations at state i , i.e., s denotes start, e denotes end, c denotes cruise, and b denotes brake.

(so that the constant relative distance could be retained). In practice, p_m^s and p_m^e are fixed due to railway safety policies. Only p_m^c and p_m^b are allowed to be optimized. Of course, p_m^c and p_m^b could also be fixed if needed or preferred. However, in this paper, we expect that the acceleration distance between p_m^s and p_m^c is as short as possible, so is the deceleration distance between p_m^b and p_m^e . This is because it is desirable for the mother train and the pilot vehicle to maintain a relative distance greater than the safety distance x_s for as long as possible. To elaborate, as depicted in Fig. 6, since x_{max} and x_s are nearly equal, extending the safety running distance between p_m^c and p_m^b implies reducing the acceleration and deceleration distances (i.e., minimizing p_m^c and maximizing p_m^b), respectively.

In summary, we solve the following multi-objective functional optimization problem, where the objectives are to minimize the acceleration distance [i.e., (3)], the deceleration distance [i.e., (4)]⁷, the total energy required [i.e., (5)], and the total jerk experienced [i.e., (6)], and the functional decision variable is the traction or braking force [i.e., $u(t)$]:

$$\min_{u(t)} p_m^c \quad (3)$$

$$\max_{u(t)} p_m^b \quad (4)$$

$$\min_{u(t)} \int_0^T |u(t) \cdot v(t)| dt \quad (5)$$

$$\min_{u(t)} \int_0^T \frac{1}{m} \left| \frac{du(t)}{dt} \right| dt \quad (6)$$

Subject to

$$\frac{dp_m}{dt} = v_m, \quad (7)$$

$$\frac{dx_{ref}}{dt} = v - v_m, \quad (8)$$

⁷We want to minimize the deceleration distance $p_m^e - p_m^b$. Since p_m^e is fixed, we just need to maximize p_m^b .

$$\frac{dv}{dt} = \epsilon \frac{u}{m} - c_0 - c_1 v - c_2 v^2 - g \sin \theta - g \frac{700}{\rho}, \quad (9)$$

$$x_{ref}|_{0 \leq p_m \leq p_m^s} = x_0, v|_{0 \leq p_m \leq p_m^s} = v_m, \quad (10)$$

$$x_{ref}|_{p_m^c \leq p_m \leq R} = x_0, v|_{p_m^c \leq p_m \leq R} = v_m, \quad (11)$$

$$x_{ref}|_{p_m^b \leq p_m \leq p_m^c} = x_{max}, v|_{p_m^c \leq p_m \leq p_m^b} = v_m, \quad (12)$$

$$p_m^s \leq p_m^c \leq p_m^b \leq p_m^e, \quad (13)$$

$$v - v_m \leq v_{max}^\Delta, \quad (14)$$

$$-\underline{U} \leq u \leq \bar{U}, u \in \mathbb{C}^0[0, T], \quad (15)$$

where $\mathbb{C}^0[0, T]$ means the collection of all continuous functions over the time period $[0, T]$. Since this is a multi-objective optimization, we can linearly combine the four objectives and solve

$$\min_{u(t)} p_m^c - p_m^b + \lambda_1 \int_0^T |u(t) \cdot v(t)| dt + \lambda_2 \int_0^T \frac{1}{m} \left| \frac{du(t)}{dt} \right| dt,$$

where $\lambda_1 \geq 0$ and $\lambda_2 \geq 0$ are trade-off weights to be empirically tuned.

Usually, we prefer to design x_{ref} with respect to p_m rather than to t because a train is always required by the train scheduling system to temporarily limit its speed or even stop, which would mess up the pre-designed running plan. Note that during a trip, T may be changed but R cannot be. Therefore, we have an alternative for the optimization problem (3)~(15) as

$$\min_u p_m^c - p_m^b + \int_0^R \lambda_1 \cdot \left| \frac{u \cdot v}{v_m} \right| + \lambda_2 \cdot \frac{1}{m} \left| \frac{du}{dp_m} \right| dp_m, \quad (16)$$

Subject to

$$\frac{dx_{ref}}{dp_m} = \frac{v}{v_m} - 1, \quad (17)$$

$$\frac{dv}{dp_m} = \frac{1}{v_m} \left[\epsilon \frac{u}{m} - c_0 - c_1 v - c_2 v^2 - g \sin \theta - g \frac{700}{\rho} \right], \quad (18)$$

Eqs. (10) ~ (15).

Note that in this case, $u \in \mathbb{C}^0[0, R]$ rather than $\mathbb{C}^0[0, T]$ because we treat u as a function of p_m instead of the time t . Note also that $|du/dt| = |du/dp_m \cdot dp_m/dt| = |du/dp_m| \cdot dp_m/dt$ because $dp_m/dt = v_m \geq 0$.

The alternative optimization problem (16) is more suitable since $\theta(\cdot)$ and $\rho(\cdot)$ are direct functions of $p := p_m + x_{ref}$. We usually set λ_2 to a large value because we expect u to be relatively smooth so that the actuator (i.e., the power system) could easily execute the command. Note that in this alternative, all the functions are with respect to p_m . In addition, according to Hölder's inequality, we have $\int_0^R |du/dp_m| dp_m \leq \sqrt{R \cdot \int_0^R (du/dp_m)^2 dp_m}$. Therefore, it suffices to replace the absolute objective function with a surrogate quadratic function (N.B.: when the L^2 norm is minimized, the L^1 norm is also decreased). This is because a smoother objective is easier to solve from the viewpoint of optimization theory. Another perspective of understanding this replacement strategy is that we use a smooth quadratic function to approximate the non-smooth absolute function; hence, one may also find other smooth functions to approximate the absolute function.

When $0 \leq p_m \leq p_m^s$, $p_m^c \leq p_m \leq p_m^b$, and $p_m^e \leq p_m \leq R$, we have $x_{ref}(\cdot)$, $v(\cdot)$ and $u(\cdot)$ as

$$\begin{cases} x_{ref}(\cdot) = x_0 \text{ or } x_{max} \\ v(\cdot) = v_m(\cdot) \\ u(\cdot) = \frac{m}{\epsilon} \left[c_0 + c_1 v + c_2 v^2 + g \sin \theta + g \frac{700}{\rho} \right], \end{cases} \quad (19)$$

since $dx_{ref}/dp_m \equiv 0$ and $dv/dp_m \equiv 0$.

Assumption 1: Suppose that

- 1) at p_m^s , the speed of the mother train reaches v_m^s ;
- 2) at p_m^c , the speed of the mother train reaches v_m^c ;
- 3) at p_m^b , the speed of the mother train reaches v_m^b ;
- 4) and at p_m^e , the speed of the mother train reaches v_m^e .

Note that $v_m^s \leq v_{m_{max}}$, $v_m^c \leq v_{m_{max}}$, $v_m^b \leq v_{m_{max}}$, and $v_m^e \leq v_{m_{max}}$, where $v_{m_{max}}$ is the speed limit of the train; for a given trip of a train, v_m^s , v_m^c , v_m^b and v_m^e are pre-determined because the speed-distance profile of the mother train is available; see Remark 4. \square

With Assumption 1, we can calculate $u_0^s := u|_{p_m=p_m^s}$, $u_0^c := u|_{p_m=p_m^c}$, $u_0^b := u|_{p_m=p_m^b}$, and $u_0^e := u|_{p_m=p_m^e}$ as

$$\begin{cases} u_0^s = \frac{m}{\epsilon} \left[c_0 + c_1 \cdot v_m^s + c_2 \cdot (v_m^s)^2 + g \sin \theta + g \frac{700}{\rho} \right] \\ u_0^c = \frac{m}{\epsilon} \left[c_0 + c_1 \cdot v_m^c + c_2 \cdot (v_m^c)^2 + g \sin \theta + g \frac{700}{\rho} \right] \\ u_0^b = \frac{m}{\epsilon} \left[c_0 + c_1 \cdot v_m^b + c_2 \cdot (v_m^b)^2 + g \sin \theta + g \frac{700}{\rho} \right] \\ u_0^e = \frac{m}{\epsilon} \left[c_0 + c_1 \cdot v_m^e + c_2 \cdot (v_m^e)^2 + g \sin \theta + g \frac{700}{\rho} \right]. \end{cases} \quad (20)$$

Therefore, the optimization problem (16) could be decomposed into two independent optimization sub-problems (21) for $p_m^s \leq p_m \leq p_m^c$ and (30) for $p_m^b \leq p_m \leq p_m^e$, in which we let $p'_m := p_m^c - p_m^s$ and $p''_m := p_m^e - p_m^b$. Note that in (21), with a slight abuse of notation, p_m no longer denotes the absolute distance to station A but the relative distance to the point p_m^s . Similarly, in (30), p_m denotes the relative distance to the point p_m^b .

$$\min_u p'_m + \int_0^{p'_m} \lambda_1 \cdot \left(\frac{u \cdot v}{v_m} \right)^2 + \lambda_2 \cdot \frac{1}{m} \left(\frac{du}{dp_m} \right)^2 dp_m, \quad (21)$$

Subject to

$$\frac{dx_{ref}}{dp_m} = \frac{v}{v_m} - 1, \quad (22)$$

$$\frac{dv}{dp_m} = \frac{1}{v_m} \left[\epsilon \frac{u}{m} - c_0 - c_1 v - c_2 v^2 - g \sin \theta - g \frac{700}{\rho} \right], \quad (23)$$

$$x_{ref}|_{p_m=0} = x_0, v|_{p_m=0} = v_m^s, \quad (24)$$

$$x_{ref}|_{p_m=p'_m} = x_{max}, v|_{p_m=p'_m} = v_m, \quad (25)$$

$$v - v_m \leq v_{max}^\Delta, \quad (26)$$

$$\left[\frac{u - u_0^s}{m} \right]^2 \leq \alpha_1 \cdot (x_{ref} - x_0), \quad (27)$$

$$\left[\frac{u - u_0^c}{m} \right]^2 \leq \alpha_2 \cdot (x_{max} - x_{ref}), \quad (28)$$

$$-\underline{U} \leq u \leq \bar{U}. \quad (29)$$

$$\min_u p''_m + \int_0^{p''_m} \lambda_1 \cdot \left(\frac{u \cdot v}{v_m} \right)^2 + \lambda_2 \cdot \frac{1}{m} \left(\frac{du}{dp_m} \right)^2 dp_m, \quad (30)$$

Subject to

$$\frac{dx_{ref}}{dp_m} = \frac{v}{v_m} - 1, \quad (31)$$

$$\frac{dv}{dp_m} = \frac{1}{v_m} \left[\epsilon \frac{u}{m} - c_0 - c_1 v - c_2 v^2 - g \sin \theta - g \frac{700}{\rho} \right], \quad (32)$$

$$x_{ref}|_{p_m=0} = x_{max}, v|_{p_m=0} = v_m, \quad (33)$$

$$x_{ref}|_{p_m=p''_m} = x_0, v|_{p_m=p''_m} = v_m^e, \quad (34)$$

$$v - v_m \leq v_{max}^\Delta, \quad (35)$$

$$\left[\frac{u - u_0^b}{m} \right]^2 \leq \alpha_2 \cdot (x_{max} - x_{ref}), \quad (36)$$

$$\left[\frac{u - u_0^e}{m} \right]^2 \leq \alpha_1 \cdot (x_{ref} - x_0), \quad (37)$$

$$-\underline{U} \leq u \leq \bar{U}. \quad (38)$$

Eqs. (27), (28), (36), and (37) are used to compel u to be continuous at $p_m = p_m^s$, $p_m = p_m^c$, $p_m = p_m^b$, and $p_m = p_m^e$, respectively, where α_1 and α_2 are scaling parameters. Taking (27) as an example for clarity, when $p'_m = x_{ref} - x_0 \geq 0$ is small, we also require that u be close to u_0^s . In contrast, when p'_m is not small, there will be no more restrictions on u because $[(u - u_0^s)/m]^2 < [u/m]^2 \leq 1$ while p'_m is usually larger than one. Note that u/m denotes the traction-weight ratio of a power system which is usually less than one. We apply the quadratic function rather than the absolute function over $(u - u_0^s)/m$ because we expect that any constraints of an optimization problem should be as smooth as possible.

The optimization problem (21) and (30) could be efficiently solved by pseudo-spectral methods. We solve them with the mature open-source PSOPT toolbox [40] developed by C++. The philosophies and theories of pseudo-spectral methods are detailed in the manual of PSOPT.

Remark 6: Suppose u^* solves the optimization problem (16). In reality, even if the pilot vehicle's power system can

exactly execute u^* , the relative distance in real time x may not follow exactly x_{ref} . This is the well-known shortness of feed-forward control methods due to the external disturbances (e.g. wind) and the modeling error of the vehicle dynamics, i.e., inexactness of the model (2). Therefore, a proper feedback control algorithm to generate u_{ref} is required. That means, this u^* does not define the u_{ref} . Instead, it is only a temporary auxiliary variable to generate x_{ref} . \square

D. Relative Distance Tracking

According to Fig. 6, we have the autonomous driving strategy for the pilot vehicle as shown in Fig. 7.

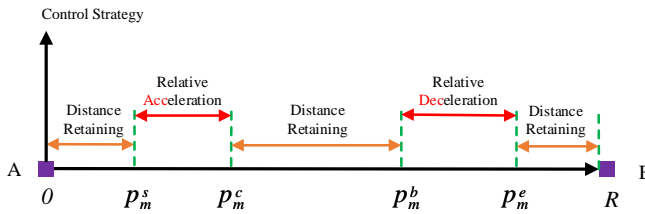


Fig. 7. Control strategy of the pilot vehicle along the track (cf. Fig. 6). The relative acceleration happens between p_m^s and p_m^c , while the relative deceleration happens between p_m^b and p_m^e . Within other sections, the relative distance remains.

Suppose that the tracking error is defined as $e(t) := x_{ref}(t) - x(t) = x_{ref}[p_m(t)] - x[p_m(t)]$. This section aims to design a proper controller that generates proper u_{ref} to eliminate the tracking error $e(t)$.

1) *Derivation of PID Controller:* Since the x_{ref} tracking problem is not a high-accuracy-required application, a properly designed PID controller is sometimes sufficient to utilize in practice. The PID controller is given as

$$u_{ref}(t) = Pe(t) + I \int_0^t e(t)dt + D \frac{de(t)}{dt}, \quad (39)$$

where P , I , and D are tunable controller parameters. In view of the space limit and novelty, details of using the PID controller could be found in Appendix C of the online supplementary materials.

2) *Alternative Controllers:* Advanced alternatives for PID controllers in railway transportation are widely studied considering tracking accuracy and many other issues or concerns; see [7, Section 3.3] for a comprehensive survey. Since this paper mainly contributes to the design of a safety guarantee system for a train operating in dangerous environments and to the design of a proper x_{ref} for autonomous driving of the pilot vehicle, we pay less attention to the advanced controller design that is mature in railway engineering. If the PID controller is not enough in some scenarios, engineers may adopt advanced alternative controllers [7], for example, Fuzzy Predictive Controller [41], [31], Fault Tolerated Controller [42], Adaptive Iterative Learning Controller [43], etc. In view of the necessity, we do not discuss this more here.

Remark 7: Due to uncertainties such as wind gusts, tunnel wind resistances, and modeling errors, in reality, the traction or braking forces u_{ref} that are truly required are sometimes greater (in absolute value) than the planned u^* to withstand

uncertainties. Therefore, \underline{U} and \bar{U} in the optimization problem (16) are actually valued less than the truly available maximum traction or braking forces. For example, if the true maximum traction force of the power system is $0.65 \times m$, we usually set $\bar{U} := 0.6 \times m$ (cf. Table I). This is one kind of conservative design strategy. Another alternative method is to consider the input-saturated control strategy [44]. \square

E. Experiments

In this subsection, we illustrate the performances of the proposed algorithms for generating and tracking x_{ref} . All the data and codes are available online at GitHub: <https://github.com/Spratm-Asleaf/Pilot-Vehicle>.

1) *Parameters and Variables:* We clarify the related parameters and their values, which we assign in experiments, in Table I, where we also summarize the immediate variables (i.e., p'_m and p''_m) and the decision variable (i.e., u) with their domains. Note that only u is the independent decision variable. p'_m and p''_m are dependent variables on u . In some railway stations, the pilot vehicle might be required to closely attach to its mother train (e.g., for the space-saving purpose); x_0 can be set to zero.

TABLE I
PARAMETERS AND VARIABLES FOR THE AUTONOMOUS DRIVING

Parameter	Description	Value
R	trip range from A to B (see Fig. 6)	300Km
p_m^s	see Fig. 6	15Km
p_m^e	see Fig. 6	$R - p_m^s$
$v_{m_{max}}$	speed limit of the mother train	120Km/h
m	mass of the pilot vehicle	2×10^3 Kg
x_s	safety distance of the train	0.8Km
x_{max}	maximum distance to retain	1.5Km
x_0	minimum distance to retain	0.1Km
g	gravitational constant, see (2)	9.80665Kg/m ²
ϵ	acceleration coefficient, see (2)	1
c_0	resistance coefficient, see (2)	0.01176
c_1	resistance coefficient, see (2)	7.7616×10^{-4}
c_2	resistance coefficient, see (2)	1.6×10^{-5}
v_{Δ}^{Δ}	maximum relative velocity, see (14)	10m/s
λ_1	see (16)	1
λ_2	see (16)	1×10^4
α_1	see (27)	1
α_2	see (37)	1
\underline{U}	maximum braking force ($\times m$)	0.5
\bar{U}	maximum traction force ($\times m$)	0.6
Variable	Description	Domain
p'_m	$:= p_m^e - p_m^s$	$[0, 6\text{Km}]$
p''_m	$:= p_m^e - p_m^b$	$[0, 6\text{Km}]$
u	traction/braking force	$[-\underline{U}, \bar{U}]$

Unit: Km stands for Kilometer, and Kg for Kilogram.

Notation: “ $\times m$ ” means “times of mass”.

As assumed in Remark 4, we already know $v_m(p_m)$ from the ATO of the train. In this experiment, we suppose that $v_m(p_m)$ is given as

$$\begin{cases} v_m = v_{m_{max}} \cdot [1 - \exp^{\beta \cdot p_m}], & 0 \leq p_m \leq p_m^s, \\ v_m = v_{m_{max}}, & p_m^s \leq p_m \leq p_m^e, \\ v_m = v_{m_{max}} \cdot [1 - \exp^{\beta \cdot (R - p_m)}], & p_m^e \leq p_m \leq R, \end{cases} \quad (40)$$

where $\beta = -0.008$ and $v_{m_{max}} = (120/3.6)\text{m/s} = 33.33\text{m/s}$. The corresponding diagram is shown in Fig. 8.

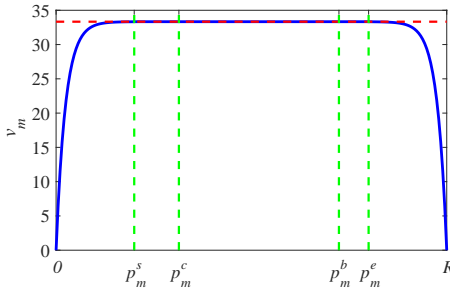


Fig. 8. Diagram of the speed profile v_m (unit: m/s) of the mother train. Red dotted line denotes $v_{m_{max}} = 33.33\text{m/s}$.

Last, we suppose that, for simplicity and without loss of generality, $\theta = \theta(p_m) \equiv 0$ and $\rho = \rho(p_m) \equiv +\infty$ along the track. It means that, in this experiment, we are investigating the railway safety guarantee problem on a flat and straight track.

2) *Results of Generating the Reference x_{ref} for x :* First, we give a summary of the results of the optimization subproblems (21) and (30) in Table II. We can see from Table II that the PSOPT can quickly solve the two problems within 6 seconds, which satisfies the real-time requirement. Furthermore, when $p_m^s \leq p_m \leq p_m^c$, the pilot vehicle takes about 5.7Km to reach x_{max} from x_0 and when $p_m^b \leq p_m \leq p_m^e$, it takes about 3.8Km to return to x_0 from x_{max} . This means $p_m^c = p_m^s + p_m' = (15 + 5.7)\text{Km} = 20.7\text{Km}$ and $p_m^b = p_m^e - p_m'' = (285 - 3.8)\text{Km} = 281.2\text{Km}$.

TABLE II
SUMMARY OF THE RESULTS OF THE OPTIMIZATIONS (21) AND (30)

Problem	Description	Value
(21)	CPU Time	5.289023 seconds
	Optimal cost function value	1.069572×10^6
	p_m'	5.718025×10^3 meters
(30)	CPU Time	5.440077 seconds
	Optimal cost function value	2.438284×10^5
	p_m''	3.798177×10^3 meters

OS: Ubuntu V22.04; GCC: V7.4.0; PSOPT: V5.0.2.

CPU: Intel(R) Xeon(R) Silver 4216 CPU @ 2.10GHz.

RAM: Samsung Synchronous-DDR4 32G.

Second, we show the generated x_{ref} in Fig. 9. We can see from Fig. 9 that the optimal command u for the optimization problem (16) is continuous and bounded as expected. It is also smooth when $p_m^s \leq p_m \leq p_m^c$ (also when $p_m^b \leq p_m \leq p_m^e$) since $\lambda_2 = 1 \times 10^4$ is large. For comparison, we also plot the optimal u for $p_m^s \leq p_m \leq p_m^c$ with $\lambda_2 = 10$ in Fig. 10. We can find that in this case, the optimal command u would not be very smooth, and so is the relative velocity profile. In addition, we study the effects of (27) and (37). If we remove (27) and (37) from the optimization subproblems (21) and (30), respectively, we have the corresponding results in Fig. 11. We can see from Fig. 11 that there are unexpected sudden changes (i.e., discontinuous points) in the optimal u .

3) *Results of Tracking the Reference x_{ref} for x :* As explained in Remark 6, the optimal **feed-forward** command u^* generated by the optimization problem (16) is different from the real reference **feedback** command u_{ref} (see also Fig. 5) fed to the power system. Because there is no feedback loop to withstand external disturbances such as wind gusts, tunnel wind resistances, and modeling errors that cause u^* to deviate from u_{ref} . Therefore, we have proposed to use a PID controller to track the expected x_{ref} in Subsection III-D. The parameters of the PID controller are $P = 0.8 \times m$, $I = 0.1 \times m$, and $D = 6 \times m$, where “ $\times m$ ” means “times of mass”.

The x_{ref} tracking performances with the PID controller are shown in Fig. 12. We can see from Fig. 12 that if given x_{ref} , the true command u_{ref} required from the power system is indeed somewhat different from u^* [cf. Fig. 9 (b)]. In addition, Fig. 12 (b) shows that the x_{ref} tracking error is within 15 meters. Since the railway safety-guarantee system does not require very high tracking accuracy of x_{ref} , the PID controller used is sufficient.

IV. VISION-BASED RAILWAY INSPECTION SYSTEM

In this section, a vision-based railway inspection system is presented to detect railway anomalies. It works with real-time images from the camera installed in front of the pilot vehicle.

A. Problem Formulation

The past decade has witnessed the great rise of Deep Convolutional Neural Networks (DCNN) in image classification [45] and object detection [46], especially for higher detection accuracy and detection rate. There were also several DCNN-based works in the maintenance of infrastructure for railway transportation systems. For example, to name a few, in [47], a DCNN-based multitask learning framework was designed for detecting defects on railway ties and fasteners; in [48], DCNN was used for wheel defects (e.g., flat spot, non-roundness, etc.) detection; in [49], a kind of track surface defect called squat was monitored based on a DCNN-type solution. As we can see, however, the reported literature has paid only attention to detecting a specific railway anomaly. We aim to provide a comprehensive solution for the detection of multiple railway anomalies, including 1) track distortion; 2) landslides and obstruction; 3) trespasser and worker, see Fig. 13. In the end, this solution is core to guaranteeing the nominal functioning of the pilot vehicle.

B. Railway Anomalies Detection Pipeline

We propose a general pipeline of vision-based railway inspection as shown in Fig. 14. The core techniques included in the pipeline are a designed architecture Folded Spatial Convolution Neural Network (FSCNN) and a track inspection algorithm based on region-of-interest (ROI) tracing. As it shows, the images are first fed into FSCNN to obtain the segmentation results of rail tracks. Based on the extracted track segments, the ROI characterized by beginning points and the vanishing point are updated in each image. Geometry extraction and anomaly inspection of the railway track are performed

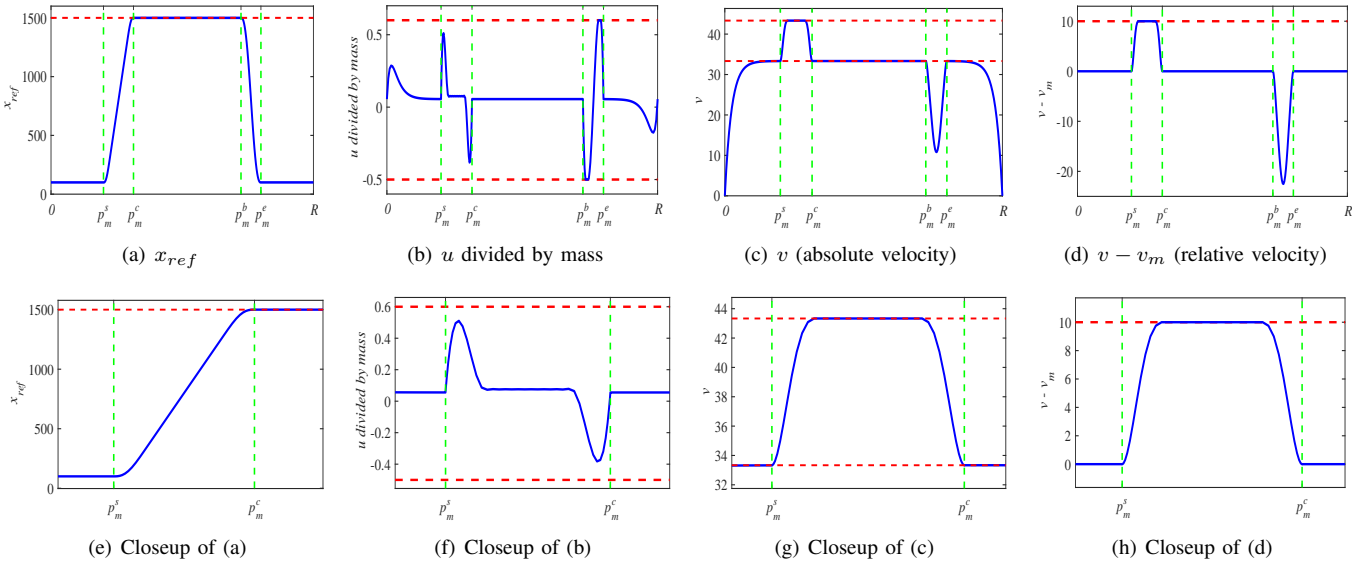


Fig. 9. Generated x_{ref} and corresponding traction/braking command u , absolute velocity v , and relative velocity $v - v_m$. Note that x_{ref} is bounded by $x_0 = 100$ and $x_{max} = 1500$; u is bounded by $\underline{U} = -0.5$ and $\overline{U} = 0.6$; v is upper bounded by $v_{max} + v_m^\Delta = [(120/3.6) + 10] \text{ m/s} = 43.33 \text{ m/s}$.

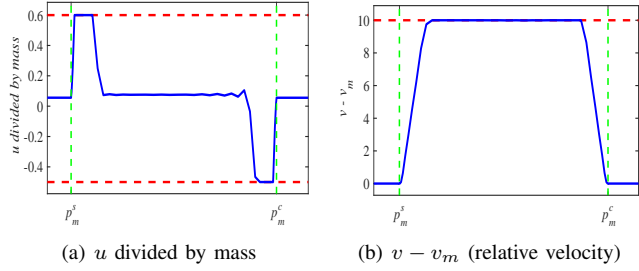


Fig. 10. Optimal u [cf. Fig. 9 (f)] and relative velocity [cf. Fig. 9 (h)] when $\lambda_2 = 10$ (cf. $\lambda_2 = 1 \times 10^4$ in Fig. 9).

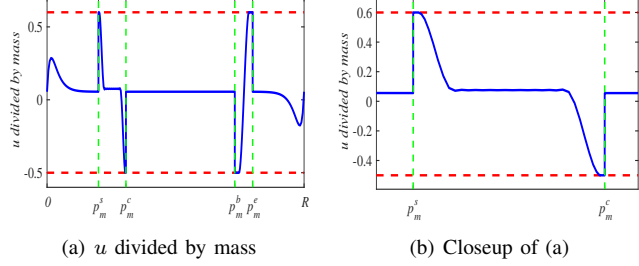


Fig. 11. Optimal u [cf. Fig. 9 (b) and (f)] when there are no continuity constraints for u .

within the latest ROI by the proposed region-growing methods. The proposed FSCNN is also used to extract the semantic segmentation results of other labels (such as trespassers, and workers) except the railway track. The following content will cover the details and results of the proposed methods.

C. Folded Spatial Convolutional Neural Networks

As the first step in implementing a railway inspection system, we propose Folded Spatial Convolutional Neural Networks (FSCNN) for the semantic segmentation of railway scenes in real-time image streams.

In an image of a railway scene, due to the long and narrow structure of railway tracks, their annotations are sparse in pixels and difficult to learn. To solve this problem, we are motivated to borrow the philosophy behind the prevailing Spatial Convolutional Neural Networks (SCNN) that perform well in lane detection for autonomous driving [51]. The SCNN was inspired by the message-passing mechanism in the conditional random field (CRF) and Markov random field (MRF) for image segmentation [51]. The message passing can be realized from four directions, namely, downward, upward, leftward, and rightward. Taking the downward message passing as an example, we have a 3-dimensional feature tensor \mathbf{F} with a size of $c_F \times h_F \times w_F$ where c_F , h_F and w_F indicate the sizes of the channel, column, and row, respectively. The feature \mathbf{F} can be divided into h_F slices of size $c_F \times w_F$ along the direction of the column, which can be represented by \mathbf{F}_i^h with $i \in [1, h_F]$. The message passing can be implemented iteratively from \mathbf{F}_1^h to $\mathbf{F}_{h_F}^h$ to produce a new feature map \mathbf{F}^D with the same sizes as \mathbf{F} . Mathematically, a convolution kernel \mathcal{K}^h with a size of $c_F \times k$ (k is the kernel size along the row, $k \leq w_F$) is involved in the downward message passing as $\mathbf{F}^D = f_{down}(\mathbf{F})$, and

$$\mathbf{F}_i^D = \begin{cases} \mathbf{F}_i^h & i = 1, \\ \mathbf{F}_i^h + [Conv(\mathbf{F}_{i-1}^h, \mathcal{K}^h)]_+ & i = 2, 3, \dots, H_F, \end{cases}$$

where $[\cdot]_+ := \max(\cdot, 0)$ is the ReLU activation function.

The core of our FSCNN is the Folded Message Passing (FMP) operation, which is the concatenation of spatial CNN features from four directions along the channel, i.e., $\mathbf{F}' = [\mathbf{F}^U, \mathbf{F}^D, \mathbf{F}^R, \mathbf{F}^L]$. Therefore, \mathbf{F}' with the sizes of $4c_F \times h_F \times w_F$ is the output of folded message passing, and \mathbf{F}^D , \mathbf{F}^U , \mathbf{F}^L , \mathbf{F}^R are the outputs of the four directional message passing operations. Subsequently, an atrous spatial pyramid pooling (ASPP) structure [52] is implemented to allow the fusion of previously concatenated outputs and adapt to the higher-level segmentation task. The objective function that we used for semantic segmentation is the widely-used

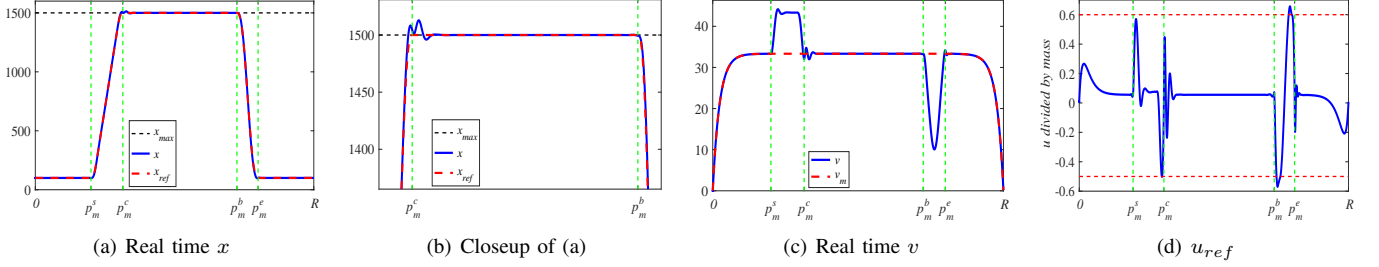


Fig. 12. Real time relative distance x under the feedback control u_{ref} . Compared with Fig. 9 (b), the **feedback** control u_{ref} here is roughly the same as the optimal **feed-forward** control u^* there, but somewhat distinct. Since the PID controller is not saturation-aware for the actuator, u_{ref} may sometimes go beyond the bounds set in Table I; cf. (d). This phenomenon can be explained by Remark 7.



Fig. 13. Three types of railway anomalies. When a pilot vehicle detects trespassers or workers, it can ring the bell to warn and expel them, or brake itself (and its mother train) to protect them. Note that braking a pilot vehicle is much easier than braking its mother train, due to mass difference.

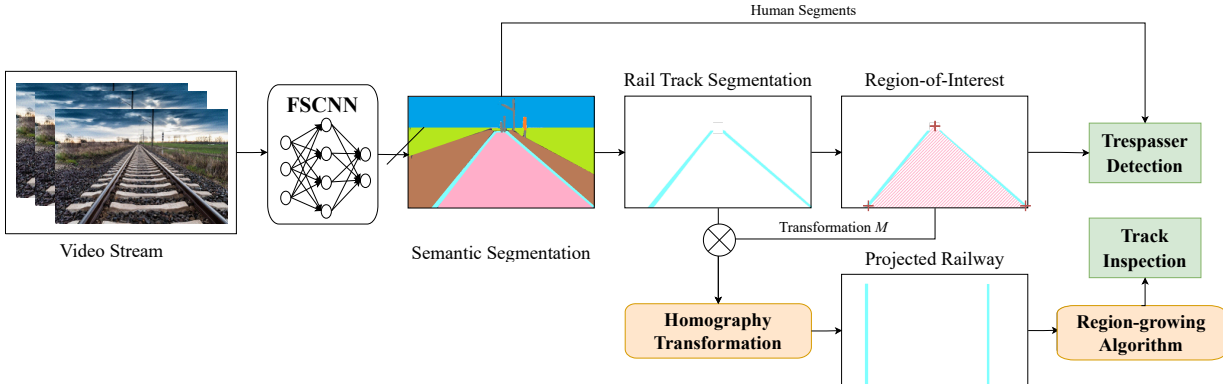


Fig. 14. The pipeline of the vision-based railway inspection system.

multi-label cross-entropy loss. The overall FSCNN model is demonstrated in Fig. 15. The advantages of our proposed FSCNN are twofold: 1) time efficiency: Instead of performing a serial four iterative directional convolutions in SCNN, we concatenate them together in parallel. This operation theoretically takes only 25% computational time of the original; 2) Powerful message passing: the message passing in SCNN is anisotropic in directions, whereas in the theoretical MRF/CRF framework influence of neighbors on a pixel should be anisotropic. Our proposed folded message-passing module can remedy this problem in a parallel way, which is followed by a convolutional operation to aggregate the directional features without sequential order.

D. Railway Track Inspection and Anomaly Detection

The proposed FSCNN can extract a binary map of railway tracks by semantic segmentation, which is further utilized for

track anomaly inspection. For these purposes, we adopt a simple yet effective pipeline including two steps: 1) Identify and trace the ROI (see Fig. 16) from the ego view of the pilot vehicle. 2) Apply a region-growing algorithm to extract and inspect railway tracks. We do not use the direct end-to-end training frame because, at present, the available annotated dataset for railway anomaly scenes is scarce. Additionally, three reasonable and practical assumptions are made:

- The train is moving smoothly in normal environments so that the ROI will not change much over a short time (More analysis is presented in Appendix D of the online supplementary materials);
- The rail track in one frame is approximately close to a straight line, i.e., not obviously winding;
- The camera is oriented in the same direction as the traveling direction.

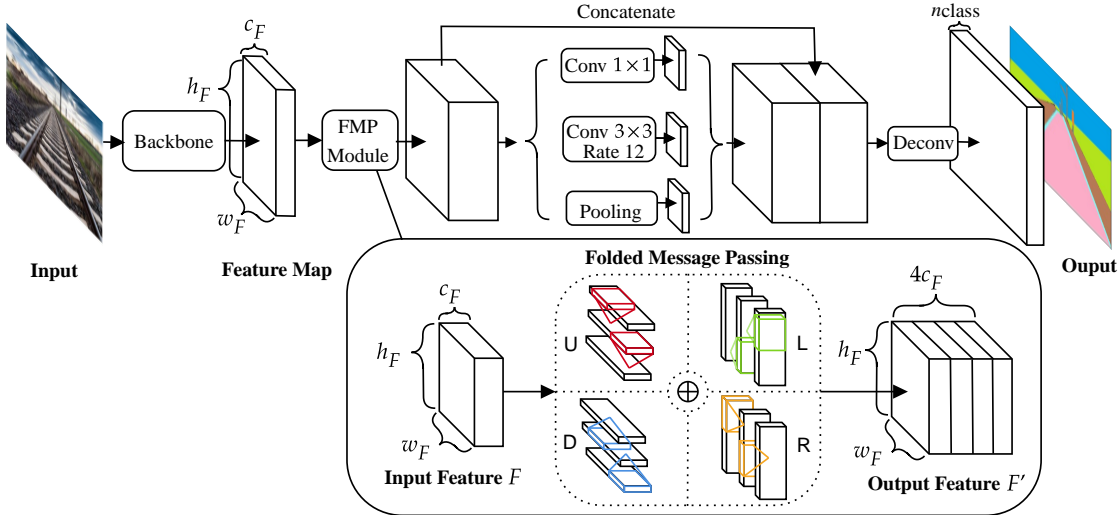


Fig. 15. The structure of FSCNN. The input of FSCNN is a railway scene image, while the output is the semantic segmentation result.

1) *Region-Of-Interest Identification and Updating*: Based on the track segmentation result in the previous step, we first identify and track ROI defined by three key points: two beginning points and one vanishing point in the image. The beginning points refer to the two initial locations where the rails emerge from the bottom of the image, while the vanishing point corresponds to the visual disappearance point of the rails. We use p_3 , p_4 , and p_0 to denote the left and right beginning points and the vanishing point, respectively, and their specific visualization is shown in Fig. 16. We then use superscripts to denote the frame number, with the superscript 0 indicating the initial frame. In general, when the camera's angle and position on the pilot vehicle are fixed, the beginning points $p_3^0 = [\mu_3^0, 0]$ and $p_4^0 = [\mu_4^0, 0]$ can be calibrated once, and their initial positions need not be changed subsequently. To update the beginning points, we perform the following operations:

$$\mu_i^t = \begin{cases} \mu_i^{t-1} & |\mu_i^{t-1} - \hat{\mu}_i^t| > \Delta_b, \\ \hat{\mu}_i^t & |\mu_i^{t-1} - \hat{\mu}_i^t| \leq \Delta_b, \end{cases}$$

where $i \in \{3, 4\}$, $\hat{\mu}_i^t$ is the closest center of track segment to μ_i^{t-1} and Δ_b is a preset neighbourhood range. The candidate centers for $\hat{\mu}_i^t$ can be extracted by contour searching [53] on the bottom pixels of the rail track segmentation binary image.

The Hough Transform (HT) [54] is used to extract the vanishing point of railway track lines. HT takes effect in a polar space equipped with two dimensions l and θ . A point in the image plane with orthogonal coordinates (μ, ν) are expressed with (l, θ) in the polar space, where $l = \mu \cos \theta + \nu \sin \theta$. By setting a proper threshold of passing points voting [54], we can extract multiple straight lines that approximate the railway tracks on images. Then, we estimate the vanishing point $p_0 = [\mu_0, \nu_0]^T$ (see Fig. 16) through a least-square method,

$$\min_{\mu_0, \nu_0} \sum_{i=1}^n a_i \cdot (l_i - \mu_0 \cos \theta_i - \nu_0 \sin \theta_i)^2, \quad (41)$$

where $a_i = z_i / \sum z_i$ and z_i is the voting number of a line (l_i, θ_i) in the polar diagram. In order to stabilize the vanishing point p_0^t in a series of images, we adopt an adaptive exponential smoothing method to eliminate the stochasticity, i.e.,

$$p_0^t = (1 - e^{-\psi \cdot \epsilon}) p_0^{t-1} + e^{-\psi \cdot \epsilon} \hat{p}_0^t, \quad (42)$$

where \hat{p}_0^t is the estimated vanishing point obtained by Hough transform in the j_{th} frame; ϵ is the residual of the least square estimation in Eq. (41) and ψ is a tunable parameter to control the weight of the current instantaneous HT estimation \hat{p}_0^t . Usually, we set $p_0^0 = \hat{p}_0^0$. Finally, we define the set of pixels located within the triangle formulated by the three key points p_0 , p_3 and p_4 as the Region of Interest i.e., ROI, denoted by \mathcal{R} . The ROI tracking method mentioned above can stably detect the same rail track across multiple frames, ensuring that the initially set track is detected even in the presence of multiple railways.

2) *Region-Growing Inspection Algorithm*: Before detecting track anomalies through the visual track segments, a homography matrix M , which transforms the visual segments from the camera's view to a bird's eye view, is determined by utilizing the ROI vertices. Given the coordinates of a railway track pixel $[\mu'_i, \nu'_i]^T$ (on an image), and the transformed bird's eye coordinate $[\mu_i, \nu_i]^T$ in the global view from above, we have $[\mu_i, \nu_i, 1]^T = M[\mu'_i, \nu'_i, 1]^T$. The basic Direct Linear Transform (DLT) algorithm [55] is applied to estimate the homography matrix M , which needs 4 point correspondences. Since we assume that the horizontal line of the image is vertical to the train's traveling direction, we can use two beginning points and two auxiliary points, which are located on the line from the beginning points to the vanishing point as the 4 correspondences. Intuitively, see Fig. 16 (c).

Next, we propose a region-growing inspection (RGI) algorithm based on the Hough transform for railway track inspection and detection from the bird eye's view. The inspection window will grow from the two beginning points. The HT algorithm is used to extract a local line segment

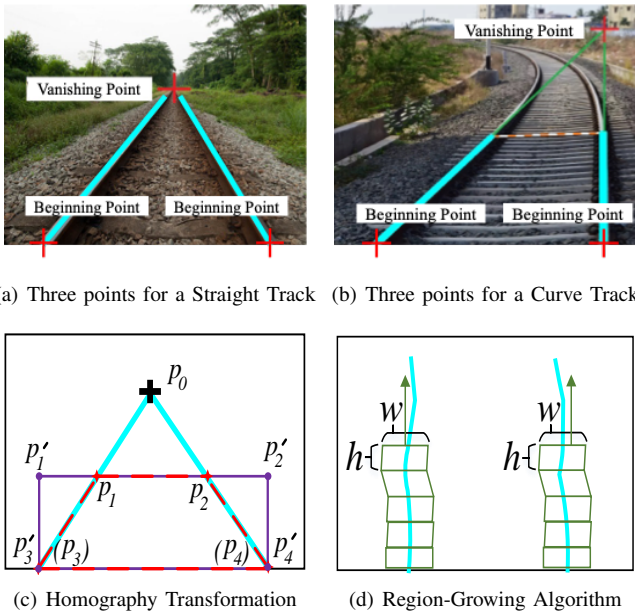


Fig. 16. An illustration of the vanishing point, beginning points, homography transformation (HoT), and region-growing algorithm. In (a) and (b), the vanishing points are marked by red crosses. In (c), p_0 is the vanishing point [cf. (a)], and HoT transforms a red dotted trapezoid (i.e., $p_1-p_2-p_3-p_4$) into a purple solid rectangle ($p'_1-p'_2-p'_3-p'_4$), and p_3 (resp. p_4) coincides with p'_3 (resp. p'_4). In (d), the tracks are projected into the bird eye's view by the homography transform. Therefore, they are parallel instead of intersecting. Note that (b) is an intra-city railway track for slow-speed trains. We choose it for demonstration because we need a significantly curving track to clearly define the VP for a curve track. For inter-city high-speed trains, curved tracks like (b) are impossible to encounter (also recall the previous assumption: railway tracks in one frame are approximately close to a straight line).

represented by $l_i = \mu \cos \theta_i + \nu \sin \theta_i$ with the largest voting point number z_i in the window. This line segment provides guidance for the growth of the next window. After defining $\mathbf{p}_a := [\mu_a, \nu_a]^\top$, $\mathbf{p}_b := [\mu_b, \nu_b]^\top$, $\mathbf{p}_c := [\mu_c, \nu_c]^\top$ and $\mathbf{p}_d := [\mu_d, \nu_d]^\top$ as four endpoints of the inspection window, we can get a new window by updating the endpoints according to Eq. (43)

$$\begin{aligned} \nu_c &= \nu_d = \tilde{\nu}_a \\ \nu_a &= \nu_b = \nu_c + h \\ \{\mathbf{p}_a, \mathbf{p}_c\} &\subset \{[\mu, \nu]^\top | l_i = (\mu - w) \cos \theta_i + \nu \sin \theta_i\} \\ \{\mathbf{p}_b, \mathbf{p}_d\} &\subset \{[\mu, \nu]^\top | l_i = (\mu + w) \cos \theta_i + \nu \sin \theta_i\} \end{aligned} \quad (43)$$

where w is the width of the window, h is the height, and $[\tilde{\mu}_a, \tilde{\nu}_a]^\top$ is the previous \mathbf{p}_a before update. Intuitively, see Fig. 16 (d). The RGI algorithm will be performed step by step until reaching an upper limiter of vertical coordinate, i.e., ν^* . Finally, the outputs of the RGI algorithm are twofold: 1) the gap $\Delta\nu^*$ between the top detected track pixel $\max \nu$ and ν^* , namely, $\Delta\nu^* = \nu^* - \max \nu$. 2) The line error $\epsilon = \sum_{j=1}^N (l_i - \mu_j \sin \theta_0 - \nu_j \cos \theta_0)^2$ in each window, where μ_j and ν_j are the coordinates of railway track pixels in the window and $\theta_0 = \pi/2$ is the vertical direction. As we can expect, the larger the error ϵ , the greater the deflection of the segmented rail from the straight line. The RGI outputs can be used to further inspect the track anomaly.

3) *Inspection Mechanism*: Based on the proposed track anomaly inspection algorithmic framework, we summarize the

mechanisms for detecting three types of anomalies during deployment. a) For track distortion anomaly, by performing the RGI algorithm, the straightness of the tracks within each window can be assessed by the line error in each window. If the error exceeds a certain threshold, the track is considered distorted. b) For landslides/obstruction anomaly, by performing the RGI algorithm, we can identify the gap $\Delta\nu^*$. If this gap exceeds a threshold, the rail is considered obstructed. c) For trespasser/worker anomaly, our approach extends the ROI to encompass a larger pixel area, which includes both the original ROI and an unsafe distance area beyond it. We then identify the semantic segments of the human category output using FSCNN. If any segment is found within the extended ROI, it indicates the presence of a trespasser. During practical deployment, it is necessary to manually set certain parameters such as the error threshold, $\Delta\nu^*$ threshold, and the safe distance. These settings are determined empirically and should be based on the railway environment and camera parameters.

E. Evaluation Dataset for Track Anomaly Inspection

To practically evaluate the performance of our vision-based anomaly inspection method, we synthesize a new evaluation dataset named RailInspect using RailSem19 [56]. Currently, there is a limited amount of research available on vision datasets specifically designed for anomaly detection in train operation scenarios, primarily due to the rarity of railroad anomalies. Previous work such as Riccardo [57] has acknowledged this challenge and collected a genuine multimodal dataset. However, the dataset has not been publicly released and focuses solely on small objects placed on the railroad track. Similarly, [58] extracted small-scale and monotonous image data from a running locomotive camera, consisting of only 120 frames of normal tracks and 12 frames of abnormal tracks. Indeed, the scarcity of the datasets presents a significant challenge in validating our proposed models and methods. To address this challenge, we propose a data augmentation framework based on the RailSem19 dataset, allowing us to simulate various dysfunctional or abnormal scenarios that can occur on real train tracks. The proposed framework enables the generation of the *RailInspect* dataset. Technically, our framework focuses on three main types of train track abnormalities: distortion, obstruction, and trespasser or worker, as depicted in Fig. 13. The specific steps involved in generating a RailInspect image are as follows:

- 1) Input: An image with pixel-wise semantic labels.
- 2) Using the method in Section IV-D1, find the ROI pixels \mathcal{R} from the railway track labels.
- 3) Determine a subset \mathcal{R}' from \mathcal{R} pixels.
- 4) Perform three types of image augmentation separately:
 - a) *Track distortion*: Distort \mathcal{R}' pixels using a ripple image distortion method with a random trigonometric function.
 - b) *Add obstacle for obstruction*: Randomly blend a random object (e.g., a big stone) at a random position on \mathcal{R}' using the mixed image blending (MIB) method.

- c) *Add human(s) as the trespasser(s) or worker(s)*: By using the MIB method, randomly blend a random human (e.g., a worker) at a random position on the extended \mathcal{R}' , which is obtained by extending a horizontal area outside the \mathcal{R}' to simulate the unsafe distance.

5) Output: Augmented images.

We chose an appropriate \mathcal{R}' to maintain a moderate distance from the pilot vehicle to the track anomaly, which is formulated as follows

$$\mathcal{R}' = \{[\mu, \nu]^\top : \nu'_{\min} \leq \nu \leq \nu'_{\max}, \forall [\mu, \nu]^\top \in \mathcal{R}\}, \quad (44)$$

$$\nu'_{\min} = \tau_1(\nu_{\max} - \nu_{\min}) + \nu_{\min}, \quad (45)$$

$$\nu'_{\max} = \tau_2(\nu_{\max} - \nu_{\min}) + \nu_{\min}, \quad (46)$$

where τ_1 and τ_2 are set to 0.3 and 0.8 in generating RailInspect, respectively, and ν_{\max} and ν_{\min} are the lower and upper vertical bound of ROI \mathcal{R} .

In the above method, the Mixed Image Blending (MIB) method combines alpha blending [59] and Poisson image editing [60]. By utilizing this combination of the two techniques, we can effectively adapt to handle various image fusion scenarios by manually adjusting the alpha parameter defined in [59]. This method enhances the flexibility of Poisson editing. Specifically, we set alpha values to 0.3 for obstruction data augmentation, while for trespasser data augmentation, the alpha value is set to 0.5.

For the ripple image distortion, we use trigonometric functions to simulate the distortion of the real track. The distorted pixel value of $[\mu, \nu]^\top \in \mathcal{R}'$ equals the original pixel value of $[\mu', \nu]^\top$, in which μ' is obtained using the trigonometric formula as follows:

$$\mu' = \mu + \frac{a_d(\nu'_{\max} - \nu)}{\nu'_{\max} - \nu'_{\min}} \sin\left(\frac{2\pi\mu}{\lambda_d}\right), \quad (47)$$

where a_d and λ_d are randomly sampled amplitude and wavelength separately to simulate various distortion scenarios.

F. Experiments and Results

All the source data and codes are available online at GitHub: <https://github.com/Spratm-Asleaf/Pilot-Vehicle>.

1) *Dataset*: For the segmentation part of the inspection system, we utilize Railsem19 [56] containing 19 categories, as our dataset to train the railway scene understanding task (i.e., semantic segmentation of railway scenes). Since [56] did not provide the dataset split, we construct our dataset by uniformly random sampling on RailSem19. A set of 4,000 images is randomly selected from RailSem19 for our experiment. The 4000 images are split into subsets of 3000, 500, and 500 images for training, validation, and testing. Furthermore, based on the techniques in Section IV-E, we constructed a balanced dataset named RailInspect-900 using the RailSem19 split test set. RailInspect-900 consists of 450 original images from the RailSem19 test set, supplemented by three augmented versions of 150 additional images obtained from the validation set, resulting in a total of 900 images. Two examples of synthesized data are showcased in Fig. 18. The RailInspect-900 is implemented to comprehensively evaluate the performance of our vision-based railway inspection system.

2) *Evaluation Metric*: For semantic segmentation of railway tracks, we calculate the intersection over-union (IoU) of the prediction of railway tracks (rail-raised and rail-embedded in RailSem19). Mathematically, the definition of IoU of a class for semantic segmentation is

$$\text{IoU}_{\text{class}} = \frac{\sum_{ij} (A_{ij}^{\text{class}} \wedge B_{ij}^{\text{class}})}{\sum_{ij} (A_{ij}^{\text{class}} \vee B_{ij}^{\text{class}})}, \quad (48)$$

where A^{class} and B^{class} are the binary segmentation masks of the predicted and ground truth sets respectively, and A_{ij}^{class} and B_{ij}^{class} are the binary values at pixel location (i, j) in the respective masks. The \wedge operator represents the logical AND, while the \vee operator represents the logical OR. The summations are performed over all pixel locations in the masks. Furthermore, the mean IoU is also calculated by averaging the IoU values for all segmented classes, i.e.,

$$\text{Mean IoU} = \sum_{\text{class} \in \text{all classes}} \text{IoU}_{\text{class}}. \quad (49)$$

Our evaluation of anomaly detection is based on the performance of methods in identifying anomaly images on the RailInspect-900 dataset. Since this is a binary classification task, we report the sensitivity (also known as Recall) of anomaly detection and the accuracy of classification. Particularly, sensitivity measures the proportion of true abnormal instances (i.e., instances that were correctly identified as abnormal) out of all the actual abnormal instances. It indicates the model's ability to correctly identify abnormal instances.

3) *Models*: For comparison of performance against our newly proposed FSCNN, we use the baseline approach proposed in [56] and the widely used SCNN architecture [51]. The backbones for SCNN and FSCNN are both ResNet50 pretrained on ImageNet dataset. All DCNN models are trained using Adam optimizer with a learning rate of 0.001. We use batch size 32 and train all models for 200 epochs. Experiments are run on a GeForce RTX 2080Ti GPU. Furthermore, to demonstrate the superiority of our anomaly inspection method, we establish a linear Support Vector Machine (SVM) based on image features as the baseline. This method utilizes a combined dataset of 4,000 randomly synthesized RailInspect images and 4,000 original images from the training set for training, where the features are extracted using the intermediate layer of a trained FSCNN.

4) *Performances of Railway Scene Segmentation*: As demonstrated in Table III, our proposed FSCNN model achieves a higher mean IoU at 62.5% than the baseline method FRRNB 56.9% and SCNN 55.0%. Because the segmentation result of rails is crucial for following railway inspections, we particularly select the Rail-raised (class 17) and Rail-embedded (class 18) in RailSem19 to show the superiority of the proposed FSCNN on long-range object segmentation task. We also provide the IoU results of other classes in Appendix E of the online supplementary materials. It is worth mentioning that FSCNN also achieves better results in other long-range classes, including Road, Tram-truck, and Rail-track. A Visualization of the railway scene understanding results is shown in Fig. 17. It can be seen that the detection of trespassers and workers, or other barriers, can be realized via

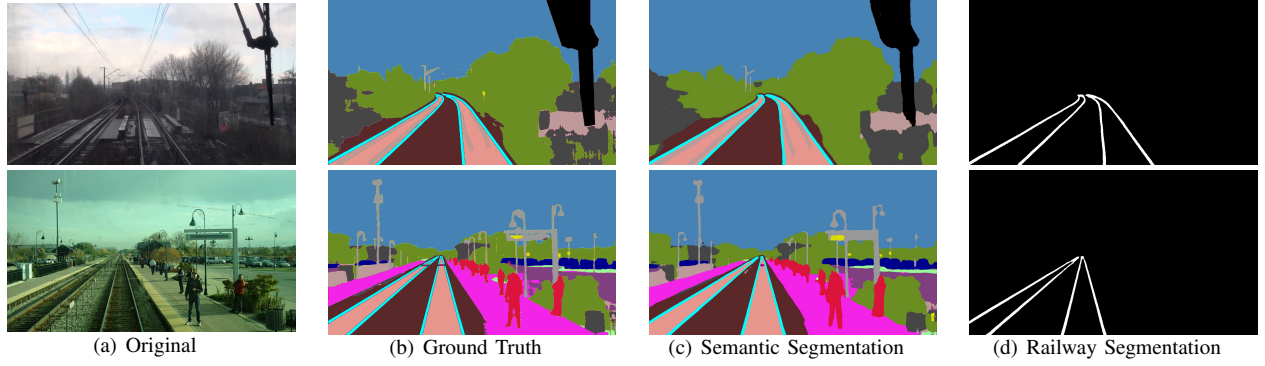


Fig. 17. The visualization of railway scene segmentation results on Railsem19 by the proposed FSCNN. The railway segmentation results are presented by binary masks of "Rail-raised" class.

the semantic segmentation results, of which the human can be well-distinguished.

TABLE III
PERFORMANCE COMPARISON AMONG DIFFERENT METHODS.

Method	Mean IoU(%)	Rail-raised IoU(%)	Rail-embedded IoU(%)
SCNN[51]	55.0	68.8	40.3
FRRNBN[56]	56.9	71.5	45.0
FSCNN(Ours)	62.5	72.4	54.2

5) *Track Anomaly Inspection*: Based on the segmentation result, we proceed to perform the track anomaly inspection on the RailInspect-900 dataset. It is worth noting that the ROI tracing method in Section IV-D1 is not exactly implemented since the utilized dataset is not based on real-time image streams. Instead, we treat each image as the first frame and use the initial steps of the algorithm in Section IV-D1 to locate the ROI. In particular, the initial beginning points are obtained from the ground truth segmentation label. A selection of the final results is visualized in Fig. 18, showcasing our approach to inspecting railway anomalies, including detecting intruders, identifying track discontinuity caused by fractures or obstacles, and recognizing track distortions. We report the specific numerical inspection results in Table IV. It can be observed from the table that our method achieves higher accuracy and sensitivity for anomaly detection compared to the data-driven baseline method. Furthermore, our detection method is capable of processing at the speed of 10 images per second, which is already applicable to practical scenarios. Concurrently, we can anticipate that by employing a more lightweight backbone, such as MobileNet [61] and using lower resolutions, the processing speed can be further improved. We leave this optimization task for future work, as the primary focus of this work is to demonstrate the feasibility of conducting anomaly inspection using vision-based approaches. Finally, we also provide a comprehensive feasibility analysis with more details in Appendix D of the online supplementary materials, further validating the potential deployment of the proposed inspection system.

TABLE IV
PERFORMANCE OF TRACK ANOMALY INSPECTION ON RAILINSPECT-900.

Method	Accuracy(%)	Sensitivity(%)		
		Distortion	Obstruction	Trespasser
FSCNN+SVM	91.3	83.3	86.7	84.7
Ours	94.0	95.3	94.7	92.0

V. CONCLUSIONS

This paper studies a safety guarantee mechanism for railway transportation systems. Specifically, it depends on a pilot vehicle as a navigator to explore the unknown railway environments ahead of the train and provide warning messages to its mother train when necessary. Related technologies, such as the autonomous driving method and the vision-based anomaly detection method, are also investigated. With this systematic approach, we expect that railway accidents worldwide could be avoided or at least controlled. Below are some closing notes.

- 1) Although railway inspection vehicles (that are independent of trains) are used to monitor the track conditions, such periodic inspections (e.g., one time per day) are not able to warn of real-time anomalies. For example, on a rainy day, the railway conditions in the morning are possible to be different from those in the evening. Therefore, the real-time railway inspection mechanism is still expected.
- 2) The proposed approach is an add-on, and therefore, a compatible solution. It does not require fundamentally changing the current railway infrastructure, for example, deploying wayside sensors or upgrading trains by installing on-board sensors.
- 3) Considering the cost-effectiveness and practical requirements, the pilot vehicle is not designated for every train in all circumstances. Instead, we suggest employing the pilot vehicle for trains operating in potentially hazardous environments, e.g., mountainous areas during rainy conditions. Different from urban transit railways that are enclosed systems and generally offer relatively safe environments, mainline railways and high-speed railways are operated in diverse and open systems, which can expose them to significantly higher risks such as trespassers and landslides [7]. Therefore, the deployment of the pilot vehicles is primarily intended for trains serving mainline railways and

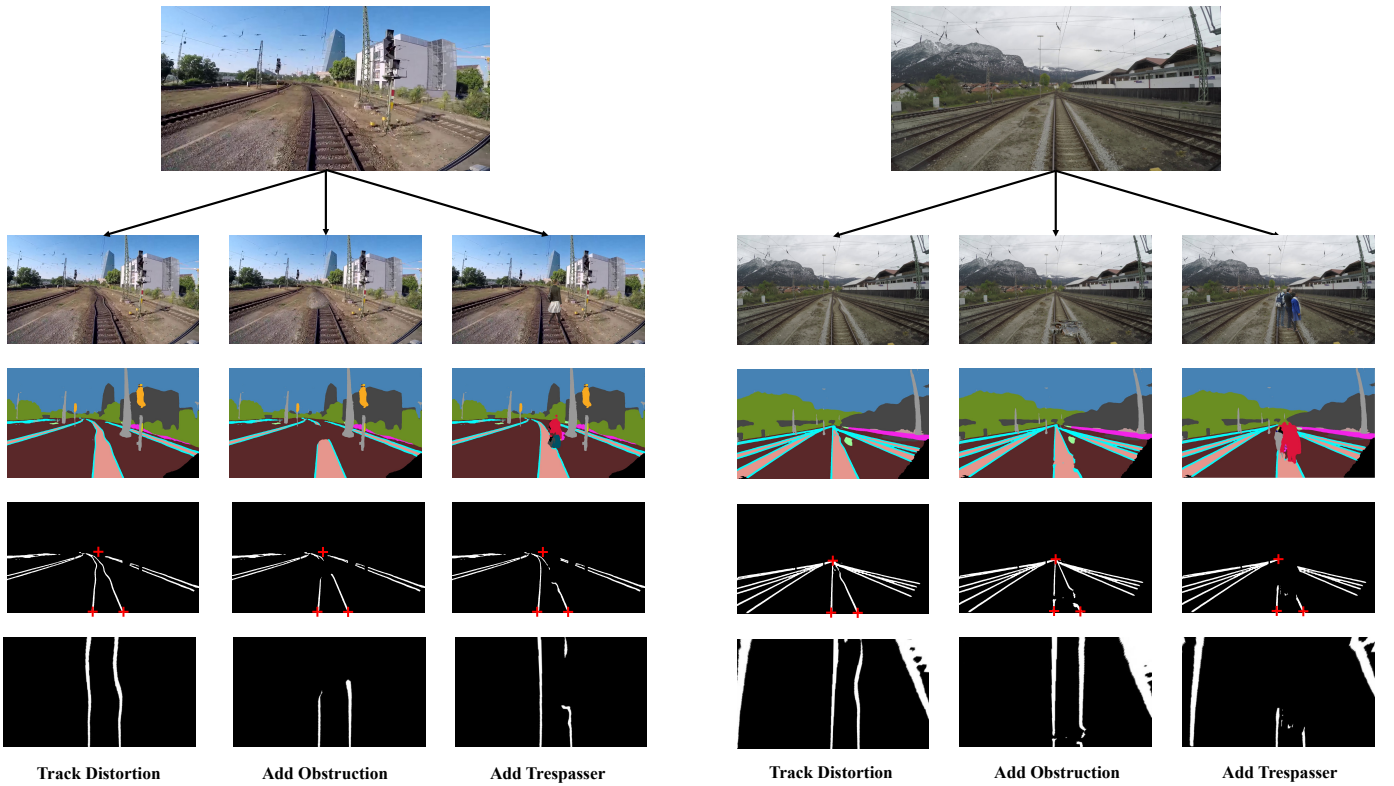


Fig. 18. The visualization of results on RailInspect-900 by the proposed railway inspection system. The rows are numbered from the top to the bottom. Row 1: two original images from RailSem-19. Row 2: the augmented images for RailInspect-900. Row 3: semantic segmentation results by FSCNN. Row 4: rail track segmentation results along with the detected vanishing point and beginning points. Row 5: projected rail track segmentation results as the input for the RGI algorithm.

high-speed railways.

- 4) It is possible that some new safety issues would be introduced when using the proposed solution. For example, the pilot vehicle might lose reliable communication with its mother train in some rare cases (e.g., anomalies in the communication devices), so the train would collide with its pilot vehicle. However, we believe that this kind of collision costs significantly less than the usual railway accidents because the mass of the pilot vehicle is small. Besides, if some buffering devices between the pilot vehicle and its mother train are used, the collision risks can be further controlled.
- 5) When the mother train is traversing or about to traverse curved segments of tracks, applying the highest braking effort can be hazardous if risk factors arise. In this situation, it is suggested to apply a more nuanced braking strategy, such as a slight reduction in speed, to mitigate the danger induced by braking on curved tracks. This strategy is essential because it allows us to minimize the impact of potential collisions with obstructions.
- 6) The vision-based railway inspection method might not work robustly at night or under extremely bad weather conditions (e.g., heavily rainy and foggy, etc.). However, it causes no disasters because we have functionally supplementary sensors to detect railway anomalies. Nevertheless, higher-performance and more robust cameras, such as LiDAR or thermal imaging [57], [62], under those conditions

are expected, as well as the corresponding rich datasets for training anomaly detection machine learning algorithms.

- 7) To the best knowledge of the authors, neither the authors nor any relevant organizations have conducted comprehensive industrial evaluations for the candidate solutions discussed in the introduction (i.e., the sensor-network-based idea, the drone-based idea, the existing SMART2 idea, and the proposed pilot-based idea). All these solutions are more academic proposals than practical implementations. Therefore, the purpose of this paper is to draw the attention of existing entities (e.g., governments, universities, and companies) to collaborate on testing potential solutions to further improve the safety of rail transportation.

For other minor closing notes, see Appendix F of the online supplementary materials.

REFERENCES

- [1] U. S. Bureau of Transportation Statistics, *National Transportation Statistics 2018*. The U.S. Department of Transportation, 2018.
- [2] Deccan-Herald, “Landslide block train movement.” <https://www.deccanherald.com/state/landslide-block-train-movement-688715.html>, 2018. Accessed on June 20, 2020.
- [3] China-Daily, “Train derails in north china, 11 dead.” http://www.chinadaily.com.cn/china/2010-08/14/content_11152712.htm, 2010. Accessed on June 20, 2020.
- [4] X. Hei, L. Chang, W. Ma, and G. Xie, “A safety framework and alarming model for train operation environment based on cps,” in *2011 Seventh International Conference on Computational Intelligence and Security*, pp. 1418–1421, IEEE, 2011.

- [5] F. Flammini, *Railway Safety, Reliability, and Security: Technologies and Systems Engineering: Technologies and Systems Engineering*. IGI Global, 2012.
- [6] J. Wang, *Safety Theory and Control Technology of High-Speed Train Operation*. Academic Press, 2017.
- [7] J. Yin, T. Tang, L. Yang, J. Xun, Y. Huang, and Z. Gao, "Research and development of automatic train operation for railway transportation systems: A survey," *Transportation Research Part C: Emerging Technologies*, vol. 85, pp. 548–572, 2017.
- [8] G. M. Scheepmaker, R. M. Goverde, and L. G. Kroon, "Review of energy-efficient train control and timetabling," *European Journal of Operational Research*, vol. 257, no. 2, pp. 355–376, 2017.
- [9] X. Yang, X. Li, B. Ning, and T. Tang, "A survey on energy-efficient train operation for urban rail transit," *IEEE Transactions on Intelligent Transportation Systems*, vol. 17, no. 1, pp. 2–13, 2015.
- [10] J. Frittelli, "Positive train control (PTC): Overview and policy issues," tech. rep., Congressional Research Service, Washington, D.C., 09 2018.
- [11] Z. Zhang, X. Liu, and K. Holt, "Positive train control (ptc) for railway safety in the united states: Policy developments and critical issues," *Utilities Policy*, vol. 51, pp. 33–40, 2018.
- [12] Y. Zhao and P. Ioannou, "Positive train control with dynamic headway based on an active communication system," *IEEE Transactions on Intelligent Transportation Systems*, vol. 16, no. 6, pp. 3095–3103, 2015.
- [13] R. D. Pascoe and T. N. Eichorn, "What is communication-based train control?," *IEEE Vehicular Technology Magazine*, vol. 4, no. 4, pp. 16–21, 2009.
- [14] Z. Zhang, C. Trivedi, and X. Liu, "Automated detection of grade-crossing-trespassing near misses based on computer vision analysis of surveillance video data," *Safety Science*, vol. 110, pp. 276–285, 2018.
- [15] S. Sharma, Y. Cui, Q. He, R. Mohammadi, and Z. Li, "Data-driven optimization of railway maintenance for track geometry," *Transportation Research Part C: Emerging Technologies*, vol. 90, pp. 34–58, 2018.
- [16] F. Marino, A. Distante, P. L. Mazzeo, and E. Stella, "A real-time visual inspection system for railway maintenance: Automatic hexagonal-headed bolts detection," *IEEE Transactions on Systems, Man, and Cybernetics, Part C (Applications and Reviews)*, vol. 37, no. 3, pp. 418–428, 2007.
- [17] G. M. Havârneanu, J.-M. Burkhardt, and F. Paran, "A systematic review of the literature on safety measures to prevent railway suicides and trespassing accidents," *Accident Analysis & Prevention*, vol. 81, pp. 30–50, 2015.
- [18] V. J. Hodge, S. O'Keefe, M. Weeks, and A. Moulds, "Wireless sensor networks for condition monitoring in the railway industry: A survey," *IEEE Transactions on intelligent transportation systems*, vol. 16, no. 3, pp. 1088–1106, 2014.
- [19] D. Ristić-Durrant, M. Franke, and K. Michels, "A review of vision-based on-board obstacle detection and distance estimation in railways," *Sensors*, vol. 21, no. 10, p. 3452, 2021.
- [20] A. S. Potdar, S. Shinde, P. H. Nikam, and M. Kurumkar, "Wireless sensor network for real time monitoring and controlling of railway accidents," in *2017 International Conference on Trends in Electronics and Informatics (ICETI)*, pp. 190–197, IEEE, 2017.
- [21] F. Flammini, A. Gaglione, F. Ottello, A. Pappalardo, C. Pragliola, and A. Tedesco, "Towards wireless sensor networks for railway infrastructure monitoring," in *Electrical Systems for Aircraft, Railway and Ship Propulsion*, pp. 1–6, IEEE, 2010.
- [22] M. A. Mahmood, W. K. Seah, and I. Welch, "Reliability in wireless sensor networks: A survey and challenges ahead," *Computer networks*, vol. 79, pp. 166–187, 2015.
- [23] J. Zhang, T. Feng, F. Yan, S. Qiao, and X. Wang, "Analysis and design on intervehicle distance control of autonomous vehicle platoons," *ISA transactions*, vol. 100, pp. 446–453, 2020.
- [24] S. Maiti, S. Winter, and L. Kulik, "A conceptualization of vehicle platoons and platoon operations," *Transportation Research Part C: Emerging Technologies*, vol. 80, pp. 1–19, 2017.
- [25] P. Hyde, C. Ulianov, J. Liu, M. Banic, M. Simonovic, and D. Ristic-Durrant, "Use cases for obstacle detection and track intrusion detection systems in the context of new generation of railway traffic management systems," *Proceedings of the Institution of Mechanical Engineers, Part F: Journal of Rail and Rapid Transit*, vol. 236, no. 2, pp. 149–158, 2022.
- [26] S. Wei, Y. Zou, X. Zhang, T. Zhang, and X. Li, "An integrated longitudinal and lateral vehicle following control system with radar and vehicle-to-vehicle communication," *IEEE Transactions on Vehicular Technology*, vol. 68, no. 2, pp. 1116–1127, 2019.
- [27] Y. Hayashi, K. S. Ram, and S. Bharule, "Handbook on high-speed rail and quality of life," tech. rep., Asian Development Bank Institute, 2020.
- [28] A. Albrecht, P. Howlett, P. Pudney, X. Vu, and P. Zhou, "The key principles of optimal train control—part 1: Formulation of the model, strategies of optimal type, evolutionary lines, location of optimal switching points," *Transportation Research Part B: Methodological*, vol. 94, pp. 482–508, 2016.
- [29] Y. Wang, B. De Schutter, T. J. van den Boom, and B. Ning, "Optimal trajectory planning for trains—a pseudospectral method and a mixed integer linear programming approach," *Transportation Research Part C: Emerging Technologies*, vol. 29, pp. 97–114, 2013.
- [30] R. Chevrier, P. Pellegrini, and J. Rodriguez, "Energy saving in railway timetabling: A bi-objective evolutionary approach for computing alternative running times," *Transportation Research Part C: Emerging Technologies*, vol. 37, pp. 20–41, 2013.
- [31] X. Wang and T. Tang, "Optimal operation of high-speed train based on fuzzy model predictive control," *Advances in Mechanical Engineering*, vol. 9, no. 3, p. 1687814017693192, 2017.
- [32] W. J. Davis, "The tractive resistance of electric locomotives and cars," *General Electric Review*, vol. XXIX, no. 10, pp. 685–707, 1926.
- [33] S. Li, L. Yang, K. Li, and Z. Gao, "Robust sampled-data cruise control scheduling of high speed train," *Transportation Research Part C: Emerging Technologies*, vol. 46, pp. 274–283, 2014.
- [34] H. Yang, Y.-T. Fu, K.-P. Zhang, and Z.-Q. Li, "Speed tracking control using an anfis model for high-speed electric multiple unit," *Control Engineering Practice*, vol. 23, pp. 57–65, 2014.
- [35] M. Güney, M. E. Korkmaz, and R. Özmen, "An investigation on braking systems used in railway vehicles," *Engineering Science and Technology, an International Journal*, vol. 23, no. 2, pp. 421–431, 2020.
- [36] G. Kitagawa and W. Gersch, *Smoothness Priors Analysis of Time Series*, vol. 116. Springer Science & Business Media, 1996.
- [37] L. I. Rudin, S. Osher, and E. Fatemi, "Nonlinear total variation based noise removal algorithms," *Physica D: Nonlinear Phenomena*, vol. 60, no. 1–4, pp. 259–268, 1992.
- [38] X. Yang, X. Li, B. Ning, and T. Tang, "A survey on energy-efficient train operation for urban rail transit," *IEEE Transactions on Intelligent Transportation Systems*, vol. 17, no. 1, pp. 2–13, 2016.
- [39] G. M. Scheepmaker and R. M. Goverde, "Energy-efficient train control using nonlinear bounded regenerative braking," *Transportation Research Part C: Emerging Technologies*, vol. 121, p. 102852, 2020.
- [40] V. M. Becerra, "Solving complex optimal control problems at no cost with psopt," in *2010 IEEE International Symposium on Computer-Aided Control System Design*, pp. 1391–1396, IEEE, 2010.
- [41] L. Zhang and X. Zhuan, "Optimal operation of heavy-haul trains equipped with electronically controlled pneumatic brake systems using model predictive control methodology," *IEEE Transactions on Control Systems Technology*, vol. 22, no. 1, pp. 13–22, 2014.
- [42] X. Yao, L. Wu, and L. Guo, "Disturbance-observer-based fault tolerant control of high-speed trains: A markovian jump system model approach," *IEEE Transactions on Systems, Man, and Cybernetics: Systems*, 2018.
- [43] D. Huang, Y. Chen, D. Meng, and P. Sun, "Adaptive iterative learning control for high-speed train: A multi-agent approach," *IEEE Transactions on Systems, Man, and Cybernetics: Systems*, 2019.
- [44] P. Lin, Y. Huang, Q. Zhang, and Z. Yuan, "Distributed velocity and input constrained tracking control of high-speed train systems," *IEEE Transactions on Systems, Man, and Cybernetics: Systems*, 2020.
- [45] C. Szegedy, W. Liu, Y. Jia, P. Sermanet, S. Reed, D. Anguelov, D. Erhan, V. Vanhoucke, and A. Rabinovich, "Going deeper with convolutions," in *Proceedings of the IEEE Conference on Computer Vision and Pattern Recognition*, pp. 1–9, 2015.
- [46] S. Ren, K. He, R. Girshick, and J. Sun, "Faster r-cnn: Towards real-time object detection with region proposal networks," in *Advances in neural information processing systems*, pp. 91–99, 2015.
- [47] X. Gibert, V. M. Patel, and R. Chellappa, "Deep multitask learning for railway track inspection," *IEEE Transactions on Intelligent Transportation Systems*, vol. 18, no. 1, pp. 153–164, 2016.
- [48] G. Krummenacher, C. S. Ong, S. Koller, S. Kobayashi, and J. M. Buhmann, "Wheel defect detection with machine learning," *IEEE Transactions on Intelligent Transportation Systems*, vol. 19, no. 4, pp. 1176–1187, 2017.
- [49] A. Jamshidi, S. Faghîh-Roohi, S. Hajizadeh, A. Núñez, R. Babuska, R. Dollevoet, Z. Li, and B. De Schutter, "A big data analysis approach for rail failure risk assessment," *Risk Analysis*, vol. 37, no. 8, pp. 1495–1507, 2017.
- [50] D. Brabie, *On the influence of rail vehicle parameters on the derailment process and its consequences*. PhD thesis, KTH, 2005.
- [51] X. Pan, J. Shi, P. Luo, X. Wang, and X. Tang, "Spatial as deep: Spatial CNN for traffic scene understanding," in *AAAI*, 2018.

- [52] L.-C. Chen, Y. Zhu, G. Papandreou, F. Schroff, and H. Adam, "Encoder-decoder with atrous separable convolution for semantic image segmentation," in *Proceedings of the European conference on computer vision (ECCV)*, pp. 801–818, 2018.
- [53] S. Suzuki *et al.*, "Topological structural analysis of digitized binary images by border following," *Computer vision, graphics, and image processing*, vol. 30, no. 1, pp. 32–46, 1985.
- [54] L. Shapiro and G. Stockman, *Computer Vision*. Prentice Hall, 2002.
- [55] R. Hartley and A. Zisserman, *Multiple View Geometry in Computer Vision*. Cambridge University Press, 2003.
- [56] O. Zendel, M. Murschitz, M. Zeilinger, D. Steininger, S. Abbasi, and C. Beleznai, "Railsem19: A dataset for semantic rail scene understanding," in *Proceedings of the IEEE/CVF Conference on Computer Vision and Pattern Recognition (CVPR) Workshops*, June 2019.
- [57] R. Gasparini, S. Pini, G. Borghi, G. Scaglione, S. Calderara, E. Fedeli, and R. Cucchiara, "Anomaly detection for vision-based railway inspection," in *Dependable Computing-EDCC 2020 Workshops: AI4RAILS, DREAMS, DSOGRI, SERENE 2020, Munich, Germany, September 7, 2020, Proceedings 16*, pp. 56–67, Springer, 2020.
- [58] K. Jahan, J. P. Umesh, and M. Roth, "Anomaly detection on the rail lines using semantic segmentation and self-supervised learning," in *2021 IEEE Symposium Series on Computational Intelligence (SSCI)*, pp. 1–7, IEEE, 2021.
- [59] T. Porter and T. Duff, "Compositing digital images," in *Proceedings of the 11th annual conference on Computer graphics and interactive techniques*, pp. 253–259, 1984.
- [60] P. Pérez, M. Gangnet, and A. Blake, "Poisson image editing," in *ACM SIGGRAPH 2003 Papers*, pp. 313–318, Association for Computing Machinery (ACM), 2003.
- [61] M. Sandler, A. Howard, M. Zhu, A. Zhmoginov, and L.-C. Chen, "Mobilenetv2: Inverted residuals and linear bottlenecks," in *Proceedings of the IEEE conference on computer vision and pattern recognition*, pp. 4510–4520, 2018.
- [62] S. Liu, Q. Wang, and Y. Luo, "A review of applications of visual inspection technology based on image processing in the railway industry," *Transportation Safety and Environment*, vol. 1, no. 3, pp. 185–204, 2019.



Dr. Shixiong Wang (Member, IEEE) received the B.Eng. degree in detection, guidance, and control technology, and the M.Eng. degree in systems and control engineering from the School of Electronics and Information, Northwestern Polytechnical University, China, in 2016 and 2018, respectively. He received his Ph.D. degree from the Department of Industrial Systems Engineering and Management, National University of Singapore, Singapore, in 2022.

He is currently a Postdoctoral Research Associate with the Intelligent Transmission and Processing Laboratory, Imperial College London, London, United Kingdom, from May 2023. He was a Postdoctoral Research Fellow with the Institute of Data Science, National University of Singapore, Singapore, from March 2022 to March 2023.

His research interest includes statistics and optimization theories with applications in signal processing (especially optimal estimation theory), machine learning (especially generalization error theory), and control technology.



Mr. Zhirui Chen obtained his bachelor's degree from Sun Yat-sen University in 2017. He is currently a Ph.D. candidate in the Department of Industrial Systems Engineering and Management at National University of Singapore. His research interests include machine learning, multi-armed bandits, and their applications.



Dr. Yang Liu is jointly appointed as an Associate Professor in the Department of Civil and Environmental Engineering and the Department of Industrial Systems Engineering and Management at the National University of Singapore, Singapore. She received her B.S. from Tsinghua University, China, MPhil from Hong Kong University of Science and Technology, Hong Kong, and Ph.D. from Northwestern University, IL, USA. Previously, Dr. Liu worked as a consultant at Cambridge Systematics. Dr. Liu's research focuses on urban mobility and

transportation systems, which covers topics in the areas of ridesharing and carsharing systems operations and design, travel demand and congestion management, and data-driven transportation system modeling and analysis. Currently, she serves on the editorial boards of *Transportation Science* (Associate Editor), *Transportation Research Part C*, and *Socio-Economic Planning Sciences* (Associate Editor). She is a co-chair of WTC Shared Logistics and *Transportation Systems Committee*, a member of *Transportation Research Board Standing Committee on Emerging and Innovative Public Transport and Technologies (AP020)* and *Transportation Network Modeling (AEP40)*, Co-Chair of Academic Affairs on the Chinese Overseas Transportation Association (COTA) Board of Directors, and a member of WCTRS Special Interest Group *Transport Theory and Modelling*.



Dr. Xinke Li received the B.Eng. degree from the College of Electronic Science and Engineering, Jilin University, China, and the M.S. degree from the Department of Electrical and Computer Engineering, National University of Singapore, Singapore. He received his Ph.D. degree from the Department of Industrial Systems Engineering and Management, National University of Singapore, Singapore. His research interests include Deep Learning for 3D vision, Graph Neural Networks, and Data-centric AI.

Supplementary Materials to “A Railway Accident Prevention System Using An Intelligent Pilot Vehicle”

Shixiong Wang, Xinkle Li, Zhirui Chen, and Yang Liu

APPENDIX A ANOTHER FORMULATION FOR GENERATING x_{ref}

In the main body of the paper, we study the formulation that minimizes the total jerk, i.e., the integral $\int_0^T \frac{1}{m} \left| \frac{du(t)}{dt} \right| dt$. To be specific, we study

$$\min_{u(t)} p_m^c - p_m^b + \lambda_1 \int_0^T |u(t) \cdot v(t)| dt + \lambda_2 \int_0^T \frac{1}{m} \left| \frac{du(t)}{dt} \right| dt \quad (1)$$

Subject to

$$\frac{dp_m}{dt} = v_m, \quad (2)$$

$$\frac{dx_{ref}}{dt} = v - v_m, \quad (3)$$

$$\frac{dv}{dt} = \epsilon \frac{u}{m} - c_0 - c_1 v - c_2 v^2 - g \sin \theta - g \frac{700}{\rho}, \quad (4)$$

$$x_{ref}|_{0 \leq p_m \leq p_m^s} = x_0, v|_{0 \leq p_m \leq p_m^s} = v_m, \quad (5)$$

$$x_{ref}|_{p_m^e \leq p_m \leq R} = x_0, v|_{p_m^e \leq p_m \leq R} = v_m, \quad (6)$$

$$x_{ref}|_{p_m^c \leq p_m \leq p_m^b} = x_{max}, v|_{p_m^c \leq p_m \leq p_m^b} = v_m, \quad (7)$$

$$p_m^s \leq p_m^c \leq p_m^b \leq p_m^e, \quad (8)$$

$$v - v_m \leq v_{max}^\Delta, \quad (9)$$

$$-\underline{U} \leq u \leq \overline{U}, u \in \mathbb{C}^0[0, T], \quad (10)$$

In this appendix, as a supplementary discussion, we study an alternative formulation, i.e., we minimize the worst-case jerk. To be specific, we investigate

$$\min_{u(t)} p_m^c - p_m^b + \lambda_1 \int_0^T |u(t) \cdot v(t)| dt + \lambda_2 \max_{0 \leq t \leq T} \frac{1}{m} \left| \frac{du(t)}{dt} \right|, \quad (11)$$

subject to (2)~(10). By introducing an auxiliary variable γ , the worst-case (i.e., min-max) jerk formulation is equivalent to

$$\min_{u(t), \gamma} p_m^c - p_m^b + \lambda_1 \int_0^T |u(t) \cdot v(t)| dt + \lambda_2 \gamma, \quad (12)$$

subject to

$$\max_{0 \leq t \leq T} \frac{1}{m} \left| \frac{du(t)}{dt} \right| \leq \gamma \quad (13)$$

$$\text{Eqs. (2) } \sim \text{(10)}. \quad (14)$$

That is,

$$\min_{u(t), \gamma} p_m^c - p_m^b + \lambda_1 \int_0^T |u(t) \cdot v(t)| dt + \lambda_2 \gamma, \quad (15)$$

subject to

$$\frac{1}{m} \left| \frac{du(t)}{dt} \right| \leq \gamma, \quad \forall t \in [0, T] \quad (16)$$

$$\text{Eqs. (2) } \sim \text{(10)}. \quad (17)$$

As explained in the main body of the paper, for technical convenience in problem-solving, we replace the absolute function with the quadratic function. We have

$$\min_{u(t), \gamma} p_m^c - p_m^b + \lambda_1 \int_0^T [u(t) \cdot v(t)]^2 dt + \lambda_2 \gamma, \quad (18)$$

subject to

$$\frac{1}{m} \left(\frac{du(t)}{dt} \right)^2 \leq \gamma, \quad \forall t \in [0, T] \quad (19)$$

$$\text{Eqs. (2) } \sim \text{ (10).} \quad (20)$$

With keeping all the shared parameters (e.g., λ_1 , λ_2 , etc.) in the experiments the same as those in the total jerk case, the experimental results of this min-max jerk formulation are given in Fig. 1. As we can see, in the min-max jerk case, the generated optimal control $u(t)$ is no longer smooth, which is not a desired property. In contrast, in the total jerk case, the generated optimal control $u(t)$ is smooth; see Fig. 9 (b) and (f) in the main body of the paper.

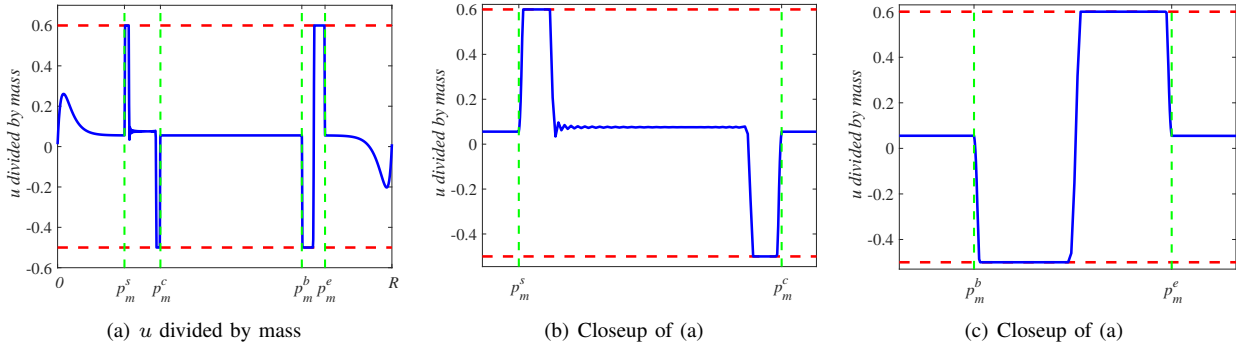


Fig. 1. Optimal u generated by the min-max formulation; cf. Fig. 9 (b) and (f) in the main body of the paper.

Remark 1: We may also suppose that the real-time jerk function is upper-bounded. That is, we may solve

$$\min_{u(t)} p_m^c - p_m^b + \lambda_1 \int_0^T |u(t) \cdot v(t)| dt, \quad (21)$$

subject to

$$\frac{1}{m} \left| \frac{du(t)}{dt} \right| \leq \theta, \quad \forall t \in [0, T] \quad (22)$$

$$\text{Eqs. (2) } \sim \text{ (10).} \quad (23)$$

where $\theta \geq 0$ is the specified upper bound of the absolute value of the jerk function. Compared to the min-max jerk case, the upper bound θ in this bounded jerk case is fixed and not expected to be minimized. This bounded-jerk formulation should be used when practitioners are confident about their knowledge of the upper bound θ . However, in terms of the smoothness of the control $u(t)$, there exists no difference between this bounded-jerk formulation and the discussed min-max jerk formulation: Both cannot guarantee the smoothness of the control $u(t)$. \square

APPENDIX B DISCUSSION ON REGENERATIVE BRAKING

There are several practical reasons why we did not consider regenerative braking technology for pilot vehicles.

- 1) First, it is true that “regenerative braking” and “automatic train operation” are mature technologies for trains [1], [2], but only for trains running in urban rail lines (i.e., metro, subway, underground system, etc.); they are not widely implemented technologies in main lines and high-speed lines [1], [3]–[8]. Note that the urban rail lines are enclosed systems, but the main lines and high-speed lines are open systems [1]. It means that the urban rail lines work in a relatively safe environment and the proposed pilot-vehicle-based accident prevention mechanism is not really necessary. Instead, as this paper claimed, we design the pilot-vehicle-based accident prevention mechanism mainly for main-line railways and high-speed railways that lie in a relatively open and diverse environment, e.g., the existence of possible mudslides and landslides, the existence of massive maintenance workers, the possibility to be trespassed by passengers, etc. In contrast, such potential dangers are rarely seen in urban rail lines: to be specific, note that urban rail lines are not in mountainous areas so that mudslides and landslides are scarce; note also that urban rail lines are greatly enclosed so that passengers are not easy to trespass.

- 2) Second, in regenerative braking, a large energy storage device is required to store energies generated by the braking process. However, according to [1, p. 568],
 “due to the high expense and limited capacity of energy storage devices, most trains in real-world applications are currently not equipped with these devices.”
- This claim can also be found in online resources such as https://energyeducation.ca/encyclopedia/Regenerative_braking.
- 3) Third, due to the maximum charging rate of the energy storage mechanisms, the braking force from a regenerative braking system (RBS) is limited. Therefore, a traditional friction brake system is still required to maintain the safe operation of a vehicle when heavy braking is necessary. Note that for a pilot vehicle, we need to reduce the deceleration distance so that most of the time, the relative distance between the mother train and the pilot vehicle is sufficiently large (i.e., the pilot vehicle can reliably provide warnings for its mother train). As a result, a heavy braking capacity is necessary for the pilot vehicle, and therefore, the regenerative braking system is not sufficient.
- 4) Fourth, the mass of a pilot vehicle is significantly small compared to a train that includes a locomotive and several carriages. That means the kinetic energy of a pilot vehicle is relatively small, and therefore, the kinetic energy wasted is greatly limited. On the other hand, not every train is deployed with a pilot vehicle. Also, a train is not always associated with a pilot vehicle in its service life. As this paper claims, a train uses a pilot vehicle ONLY when it runs in mountainous areas during rainy days. As such, the kinetic energy wasted is further limited.
- 5) Fifth, deploying the extra equipment (i.e., the regenerative braking system) on the pilot vehicle means the extra significant mass, which, on the contrary, improves the energy consumption in the acceleration and cruise stages. Hence, there exists a trade-off between the amount of saved energy and the amount of extra consumed energy; for more information, see https://energyeducation.ca/encyclopedia/Regenerative_braking. As such, we leave the issue (of whether to deploy the regenerative braking system on the pilot vehicle) to practitioners who implement the proposed accident prevention mechanism.
- 6) Sixth, the main focus of this paper is to design the pilot-vehicle-based accident prevention scheme. Other detailed and advanced technologies in implementation deserve independent scientific research or engineering practice.

APPENDIX C DERIVATION OF PID CONTROLLER

Since the x_{ref} tracking problem is not a high-accuracy-required application, a properly designed PID controller is sometimes sufficient to utilize in practice. The PID controller is given as

$$u_{ref}(t) = Pe(t) + I \int_0^t e(t)dt + D \frac{de(t)}{dt}, \quad (24)$$

where P , I , and D are designed controller parameters. Therefore, incorporating (24) into the system dynamics of the pilot vehicle, the whole system dynamics becomes

$$\left\{ \begin{array}{l} \frac{dp_m}{dt} = v_m \\ \frac{dx}{dt} = v - v_m \\ \frac{dv}{dt} = \epsilon \frac{u_{ref}}{m} - c_0 - c_1 v - c_2 v^2 - g \sin \theta - g \frac{700}{\rho} \\ \frac{du_{ref}}{dt} = P \frac{d(x_{ref} - x)}{dt} + I(x_{ref} - x) + D \frac{d^2(x_{ref} - x)}{dt^2}, \end{array} \right. \quad (25)$$

with initial conditions $p_m|_{t=0} = 0$, $x|_{t=0} = x_0$, $v|_{t=0} = v_m|_{t=0} = 0$ and $u_{ref}|_{t=0} = 0$. In (25), $v_m(t)$ and $x(t)$ are obtained from the corresponding sensing devices and fed to the controller directly. Recall that x_{ref} is directly a function of p_m (see Subsection III-C in the main body of the paper) and indirectly a function of the time t .

Eq. (25) in the present form is not a standard form of ordinary differential equations (ODEs) because time derivatives are involved in the right-hand-side of the ordinary differential equation du_{ref}/dt . Besides, we do not know the values of dx_{ref}/dt and d^2x_{ref}/dt^2 . For a real application, it does not matter since we can use (24) to generate control signal $u_{ref}(t)$ directly. However, for the simulation study in this paper, we need to transform it into a standard one so that we can invoke standard ODEs solvers, e.g., Runge–Kutta methods. Since

$$\frac{dx_{ref}}{dt} = \frac{dx_{ref}}{dp_m} \cdot \frac{dp_m}{dt} = v_m \cdot \frac{dx_{ref}}{dp_m}, \quad (26)$$

$$\frac{d^2x}{dt^2} = \frac{d(\frac{dx}{dt})}{dt} = \frac{dv}{dt} - \frac{dv_m}{dt} = \frac{dv}{dt} - v_m \cdot \frac{dv_m}{dp_m}, \quad (27)$$

and

$$\frac{d^2x_{ref}}{dt^2} = \frac{d(\frac{dx_{ref}}{dt})}{dt} = \frac{d(v_m \cdot \frac{dx_{ref}}{dp_m})}{dp_m} \cdot v_m = v_m \cdot \frac{dv_m}{dp_m} \cdot \frac{dx_{ref}}{dp_m} + v_m^2 \cdot \frac{d^2x_{ref}}{dp_m^2}, \quad (28)$$

we have

$$\frac{du_{ref}}{dt} = P \left[v_m \cdot \frac{dx_{ref}}{dp_m} - \frac{dx}{dt} \right] + I [x_{ref} - x] + D \left[v_m \cdot \frac{dv_m}{dp_m} \frac{dx_{ref}}{dp_m} + v_m^2 \cdot \frac{d^2x_{ref}}{dp_m^2} - \frac{dv}{dt} + v_m \cdot \frac{dv_m}{dp_m} \right]. \quad (29)$$

Eq. (29) transforms (25) into a standard form of ODEs which could be solved by standard solvers. Note that the values of dx/dt and dv/dt are available from (25) and x and v_m are from sensing devices. Note also that x_{ref} , dx_{ref}/dp_m , dv_m/dp_m , and d^2x_{ref}/dp_m^2 are available from the design procedure (see Subsection III-C in the main body of the paper).

APPENDIX D FEASIBILITY ANALYSIS OF VISION-BASED TRACK INSPECTION SYSTEM

Due to the prohibitively high costs and insurmountable constraints, it is intractable for us to validate the feasibility of our visual railway inspection system through real-world deployment. Nevertheless, we still provide a mathematical model analysis incorporating realistic parameters in the following content. The analysis starts by imaging system analysis based on imaging distance and quality, followed by

A. Imaging System

Imaging Distance. We define two distances related to the track inspection system. Lens working distance d_w : the distance between the front surface of the lens and the nearest point of the object being imaged that is in focus. Emergency Braking Distance d_p : the distance that a train experiences when it brakes itself with its highest braking efforts. To make sure that the pilot vehicle can react to the inspected anomaly promptly, the distances must follow $d_p \leq d_w$. The calculation of d_p is proposed in Sec. D-B. In practice, we can simply increase the focal length of the camera lens (i.e., zoom in) to obtain a large d_w . A simulated example of zoom-in image is illustrated in Fig. 3. It shows that by adjusting the camera lens carefully, we can obtain a distant view of the railway that is similar to images from the RailSem19 dataset. Moreover, it is not necessary to re-adjust the camera since the pixel location of the rail track will not shift obviously during the operation process, which is demonstrated in Sec. D-C.

Image Quality. We are also concerned with ensuring image quality to enhance the ability of the inspection system. Specifically, in high-speed railway scenarios, image quality is primarily constrained by two factors: depth of field (DOF) and motion blur. The DOF refers to the range of sharpness in a photograph or image, where objects farther or closer than the working distance appear blurred. To calculate the DOF, the near limit (NL), which is the closest distance at which objects appear sharp, and the far limit (FL), which is the furthest distance at which objects appear sharp, must be computed. The NL can be obtained by

$$NL = \frac{d_w f_l^2}{f_l^2 - k_f \delta_c (d_w - f_l)},$$

and FL can be obtained by

$$FL = \frac{d_w f_l^2}{f_l^2 + k_f \delta_c (d_w - f_l)},$$

where f_l is the focal length of the lens, k_f is the aperture (f-number), and δ_c is the circle of confusion, which is the maximum acceptable diameter of a blur circle in the image plane for it to be considered sharp. Suppose a common setting of cameras and lens, which includes $k_f = 2.8$, $d_w = 100m$, $f_l = 0.3m$ and $\delta_c = 3.5 \times 10^{-5}m$, we can obtain 90.18m of NL and 112.21m of FL.

Furthermore, motion blur is a photographic effect that occurs when a moving object is captured over time, resulting in a blurred appearance. To overcome motion blur due to the high speed of the train, we propose using the latest high-speed imaging techniques. Some examples of commercial products of these high-speed cameras are presented in Tab. I. The FPS (frames per second) of a camera greater than 1000 makes it possible to capture clear anomaly images on a high-speed vehicle. In addition, a complementary solution for motion blur is to use a high-intensity strobe light source for exposure [9], which can also be useful for night vision.

TABLE I
EXAMPLES OF HIGH-SPEED IMAGING CAMERAS

Name	Brand	Maximum Resolution (pixels)	Acquisition Speed (FPS)
PHANTOM Miro C320 High-Speed Camera ¹	Darwin Microfluidics	1920 × 1080	1480
SMI-UHS-1024P-05 ²	SmartMoreInside	2048 × 1024	2000
Falcon4-CLHS M2240 ³	Teledyne DALSA	2240 × 1248	1200

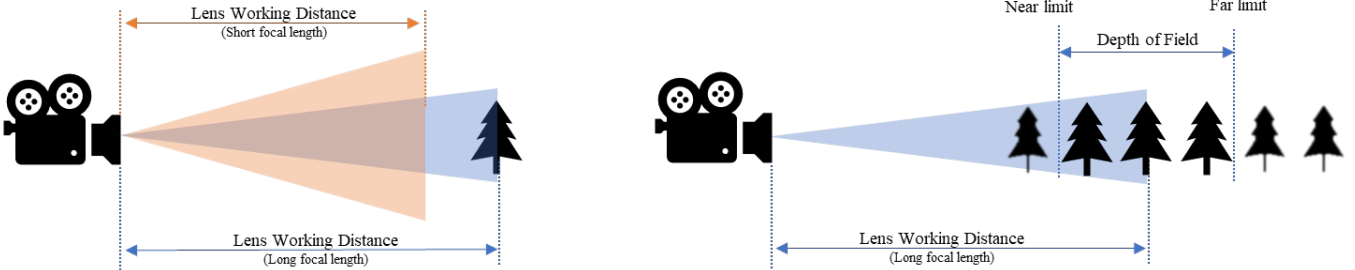


Fig. 2. Visualization of the concepts in the imaging system including lens working distance, depth of field, near limit, and far limit.



Fig. 3. A simulated visualization of increasing the focal length of the camera in a railway scene.

B. Emergency Braking Distance.

Suppose the speed of the pilot (when the pilot sees a rail anomaly) is v , the anomaly identification time of the pilot is t_i (N.B. it takes time to identify an anomaly after seeing it due to vision processing delay), and the emergency braking deceleration of the pilot is b_p . Then, the emergency braking distance of the pilot is

$$d_p = vt_i + v \left(\frac{v}{b_p} \right) - \frac{1}{2} b_p \left(\frac{v}{b_p} \right)^2 = vt_i + \frac{1}{2} \frac{v^2}{b_p}.$$

According to the visual processing results, we have $t_i = 0.1s$. Let $b_p = 3 \times 9.8m/s^2$ (i.e., three times of gravitational acceleration). Since the mass of a pilot is relatively small and there is no human inside a pilot, a pilot can tolerate a much larger braking deceleration compared to a usual train. Assume $v = 70m/s$ (i.e., 250Km/h), which is a high speed in dangerous areas (e.g., mountainous areas during rainy days); see https://en.wikipedia.org/wiki/High-speed_rail. Finally, we have the expected distance $d_p = 88.96m$ and have to ensure that $d_w \geq 88.96m$. By implementing the setting of $d_w = 100m$ in Appendix D-A, we can obtain a clear imagery view from 90.18m to 112.21m in which interval any value is larger than d_p .

C. Lateral Shift of Track on Image.

It is noted that curved tracks shift laterally from their original vertical alignment on the image. This track shift has the potential to cause the rail tracks to move out of the camera's field of view, making it challenging for anomaly detection. The following content discusses this effect. Consider a curved track as illustrated in Fig. 4. A curved track that has a length of the lens working distance d_w (e.g., segment PC) can be seen as straight. This is because the curvature radius ρ (i.e., the line segment AO) is significantly larger than d_w . Mathematically, the lateral shift of track on d_w location is given by

$$\text{lateral shift DC} = \rho - \sqrt{\rho^2 - PC^2}$$

To be quantitatively specific, supposing $d_w = 100m$ as calculated above and $\rho = 2000m$ for a high-speed line (see https://en.wikipedia.org/wiki/Minimum_railway_curve_radius), we have $DC = 2.5m$. By assuming a resolution of 100pixels/m on the bottom horizontal pixels of a 1920×1080 image, which is a typical value in the RailSem19 dataset, the actual track shift

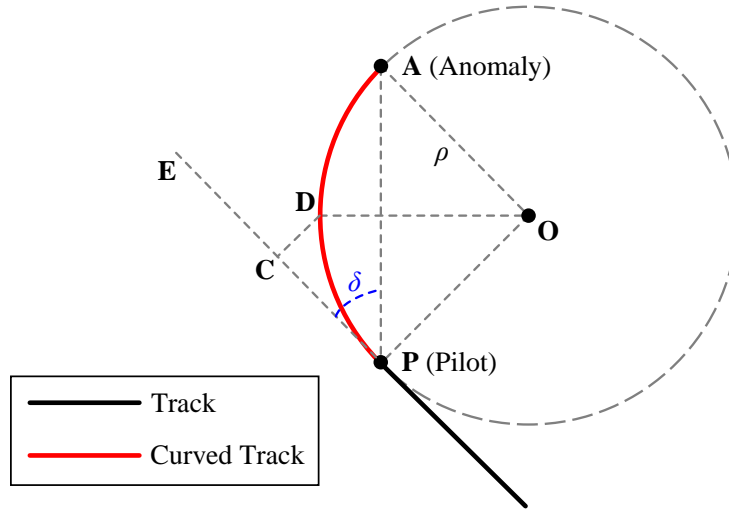


Fig. 4. A short curved track segment (e.g., the arc segment ADP) can be seen as straight since the angle δ of sight is small.

will result in a 250-pixel shift in the image. We note that it is straightforward to ensure that the pixel shift does not cause the rail track to move out of the image by positioning the track in the center of the image.

Furthermore, we consider Δ_d of beginning points tracking in Section IV.D in the main context. Δ_d refers to the maximum pixel distance of beginning points laterally shift between two frames. By assuming the 70m/s of vehicle speed and 0.1s frame processing time, we can obtain the 7m of forward distance for the pilot between two processed frames. Thus, we have $DC = 0.012\text{m}$ and 1.2-pixel shift based on the above parameter settings. This is a quite small number indicating that the beginning points change is tiny during operation. Finally, we can set Δ_d to be a small number, namely, 10 pixels, for beginning points tracking.

APPENDIX E MORE RESULTS OF VIDEO-BASED INSPECTION SYSTEM

TABLE II
COMPARISON OF IOU(%) RESULTS ON RAILSEM19 SEMANTIC SEGMENTATION TASK. (C_i IS THE i_{th} CLASS IN RAILSEM19 DATASET.)

Method	C_1	C_2	C_3	C_4	C_5	C_6	C_7	C_8	C_9	C_{10}
SCNN	48.1	52.2	70.2	47.3	46.7	59.4	34.3	29.5	83.9	54.6
FRRNB	50.5	54.0	72.4	40.1	49.8	60.2	36.8	32.5	84.1	59.5
FSCNN	53.4	53.1	71.7	70.2	47.0	62.6	45.6	44.5	84.1	61.9
Method	C_{11}	C_{12}	C_{13}	C_{14}	C_{15}	C_{16}	C_{17}	C_{18}	C_{19}	
SCNN	94.2	45.9	79.5	48.7	18.1	63.9	60.5	68.8	40.3	
FRRNB	94.7	46.7	81.9	50.6	20.7	67.8	62.8	71.5	45.0	
FSCNN	95.8	63.6	89.2	73.1	16.2	72.5	56.7	72.4	54.2	

APPENDIX F CLOSING NOTES

In this appendix, we provide some closing notes to clear possible confusion from readers.

- 1) The distances between different adjacent stations are different, leading to different curves of x_{ref} . For this reason, we need to separately design x_{ref} for every two adjacent stations. We just need to plug in the required parameters such as the distance between the two adjacent stations. Then, we can quickly get a specific x_{ref} for the two considered adjacent stations. The computational time of x_{ref} is generally speaking short, just in several seconds; cf. Table II in the experiments in Subsection III-E (title: Experiments). Hence, planning a x_{ref} for every two adjacent stations is computationally easy, which can be done even just before the train is to depart from the starting station.
- 2) Note that it is the pilot vehicle that dynamically adjusts its relative distance to the mother train. The running plan of the mother train is determined by the Train Scheduling System and is not to be changed by the proposed safety-guaranteeing sub-system. See Remark 4 in the main body of the paper. The x_{ref} is always pre-designed for every two adjacent stations. Hence, during the running of the mother train, the pilot vehicle just uses its power system to generate proper traction and braking forces, and these proper forces allow the real-time relative distance between the train and the pilot to track x_{ref} . In this tracking process, feedback control is necessary, as discussed in Subsection III-D (title: Relative Distance Tracking).

- 3) As for the moving blocks and/or positive train control issues, they do not influence the design of x_{ref} because the designed x_{ref} is a function of the position p_m of the mother train (cf. Figure 6 in the main body of the paper), NOT a function of the time. To be more specific, when moving blocks and/or positive train control commands require the mother train to stop, the pilot vehicle will also stop because it needs to maintain the distance x_{ref} from the mother train. When the mother train continues running after moving blocks and/or positive train control, the pilot vehicle will also continue running because it needs to maintain the distance x_{ref} from the mother train. This is a benefit of using the feedback control. Note that the stopping/running strategies of the mother train are made by the Train Scheduling System when there exist moving blocks and/or positive train control commands. But this does not influence the running of the pilot vehicle because the pilot vehicle needs to maintain the distance x_{ref} from the mother train. **When the train stops (resp. runs), the pilot also stops (resp. runs).** The only difference is that when the Train Scheduling System makes stopping/running commands for a train due to moving blocks and/or positive train control, the position of the pilot vehicle should also be considered. This is practically easy to implement because we can just treat a train-pilot grouping as a long and multi-unit train. Namely, a pilot vehicle can be seen as a part of a train, e.g., a virtual locomotive.
- 4) When we design a target distance-speed profile of a mother train (based on moving authority or the service braking curve), we DO NOT consider any emergency situations—we just assume there will NOT exist emergency situations when the train is running according to its pre-designed distance-speed profile. We do not know where the emergency situations will happen along the track, and therefore, it is not practical to design a distance-speed profile for a mother train that takes into consideration of emergency situations. Note that only when we exactly know the positions where the emergency situations happen can we design a so-called target distance-speed profile for braking. Therefore, for the purpose of safety-guaranteeing, the good practice is to use a safe value for the emergency braking distance (i.e., x_s in Figure 6 in the main body of the paper) and let the mother train brake itself as quickly as possible with its highest effort (i.e., using the largest braking force) whenever an emergence is detected.
- 5) The designed scheme in this paper is more an academic blueprint than a practically validated solution: As a single university, it is difficult for us to make and implement such a pilot vehicle to verify the proposed solution because considerable railroad hardware and facilities are expected to be involved. For example, the cost-benefit analyses of the Positive Train Control (PTC) scheme were conducted by the US government where several universities and companies participated; see Page 12 of the literature

Peters, J. C., & Frittelli, J. (2018). Positive Train Control (PTC): Overview and Policy Issues.

Also, to the best knowledge of the authors, neither the authors nor any relevant organizations have conducted specific evaluations for the above candidate solutions—all these solutions are more academic proposals than practical implementations. Therefore, the purpose of this paper is to draw the attention of existing entities (e.g., governments, universities, and companies) to collaborate on testing potential solutions (e.g., the sensor-network-based idea, the drone-based idea, the existing SMART2 idea, the proposed pilot-based idea) to further improve the safety of rail transportation. (For the review of the sensor-network-based idea, the drone-based idea, and the SMART2 idea, see the Introduction.) In other words, we would like to leave detailed, commercial, and financial cost-benefit analyses and verification to our industrial colleagues. We hope that this does not influence the completeness of this paper.

- 6) We clarify that the situation detection camera must be installed on the pilot vehicle, not the mother train. This is because the effective visual detection distance of a camera is significantly smaller than the emergency braking distance of the mother train. Hence, if the camera is mounted on the mother train and when the railway anomaly (e.g., landslides) is detected by the camera, it is already too late for the mother train to brake itself. In contrast, if the camera is installed on the pilot vehicle and when the railway anomaly is detected by the camera, the mother train has a sufficient buffering distance to brake itself. Note that the relative distance between the pilot vehicle and the mother train is maintained to be larger than the emergency braking distance; see Figure 6 in the main body of the paper. In terms of the pilot vehicle, it has significantly lighter weight than its mother train, which results in a shorter brake distance that can be covered by the range of the visual inspection system. In other words, whenever a railway anomaly is detected by the camera, the pilot vehicle can completely brake itself before reaching the anomaly because it has a small inertia; see also Appendix D.

REFERENCES

- [1] J. Yin, T. Tang, L. Yang, J. Xun, Y. Huang, and Z. Gao, "Research and development of automatic train operation for railway transportation systems: A survey," *Transportation Research Part C: Emerging Technologies*, vol. 85, pp. 548–572, 2017.
- [2] A. Albrecht, P. Howlett, P. Pudney, X. Vu, and P. Zhou, "The key principles of optimal train control—part 1: Formulation of the model, strategies of optimal type, evolutionary lines, location of optimal switching points," *Transportation Research Part B: Methodological*, vol. 94, pp. 482–508, 2016.
- [3] M. Domínguez, A. Fernández-Cardador, A. P. Cucala, and R. R. Pecharromán, "Energy savings in metropolitan railway substations through regenerative energy recovery and optimal design of ato speed profiles," *IEEE Transactions on Automation Science and Engineering*, vol. 9, no. 3, pp. 496–504, 2012.
- [4] A. González-Gil, R. Palacin, and P. Batty, "Sustainable urban rail systems: Strategies and technologies for optimal management of regenerative braking energy," *Energy Conversion and Management*, vol. 75, pp. 374–388, 2013.
- [5] X. Yang, A. Chen, X. Li, B. Ning, and T. Tang, "An energy-efficient scheduling approach to improve the utilization of regenerative energy for metro systems," *Transportation Research Part C: Emerging Technologies*, vol. 57, pp. 13–29, 2015.
- [6] X. Yang, X. Li, B. Ning, and T. Tang, "A survey on energy-efficient train operation for urban rail transit," *IEEE Transactions on Intelligent Transportation Systems*, vol. 17, no. 1, pp. 2–13, 2016.

- [7] G. M. Scheepmaker and R. M. Goverde, "Energy-efficient train control using nonlinear bounded regenerative braking," *Transportation Research Part C: Emerging Technologies*, vol. 121, p. 102852, 2020.
- [8] W. Zhou, Y. Huang, L. Deng, and J. Qin, "Collaborative optimization of energy-efficient train schedule and train circulation plan for urban rail," *Energy*, vol. 263, p. 125599, 2023.
- [9] P. J. Sousa, F. Carneiro, N. V. Ramos, P. J. Tavares, and P. M. Moreira, "Development of led-based illumination system for high-speed digital image correlation," *Procedia Structural Integrity*, vol. 17, pp. 828–834, 2019.